The Astrophysical Journal, 632:58–80, 2005 October 10

EXPANSION AND COLLAPSE IN THE COSMIC WEB[1,2]

Michael Rauch,[3] George D. Becker,[4] Matteo Viel,[5] Wallace L. W. Sargent,[4] Alain Smette,[6,7]
Robert A. Simcoe,[8] Thomas A. Barlow,[4] and Martin G. Haehnelt[5]

Received 2005 April 2; accepted 2005 May 26

ABSTRACT

We study the kinematics of the gaseous cosmic web at high redshift using Lyα forest absorption in multiple QSO sight lines. Observations of the projected velocity shifts between Lyα absorbers common to the lines of sight to a gravitationally lensed QSO and three more widely separated QSO pairs are used to directly measure the expansion of the cosmic web in units of the Hubble velocity, as a function of redshift and spatial scale. The lines of sight used span a redshift range from about 2 to 4.5 and represent transverse scales from the subkiloparsec range to about 300 h_{70}^{-1} physical kpc. Using a simple analytic model and a cosmological hydrodynamic simulation, we constrain the underlying three-dimensional distribution of expansion velocities from the observed line-of-sight distribution of velocity shear across the plane of the sky. The shape of the shear distribution and its width (14.9 km s^{-1} rms for a physical transverse separation of 61 h_{70}^{-1} kpc at $z = 2$, 30.0 km s^{-1} for 261 h_{70}^{-1} kpc at $z = 3.6$) are found to be in good agreement with the IGM undergoing large-scale motions dominated by the Hubble flow, making this one of the most direct observations possible of the expansion of the universe. However, modeling the Lyα clouds with a simple "expanding pancake" model, the average expansion velocity of the gaseous structures causing the Lyα forest in the lower redshift ($z \sim 2$) smaller separation (61 kpc) sample appears about 20% lower than the local Hubble expansion velocity.

In order to understand the observed velocity distribution further we investigated the statistical distribution of expansion velocities in cosmological Lyα forest simulations. The mean expansion velocity in the ($z \sim 2$, separation $\sim$ 60 kpc) simulation is indeed somewhat smaller than the Hubble velocity, as found in the real data. We interpret this finding as tentative evidence for some Lyα forest clouds breaking away from the Hubble flow and undergoing the early stages of gravitational collapse. However, the distribution of velocities is highly skewed, and the majority of Lyα forest clouds at all redshifts from 2 to 3.8 expand with super-Hubble velocities, typically about 5%–20% faster than the Hubble flow. This behavior is explained if most Lyα forest clouds in the column density range typically detectable are expanding filaments that stretch and drain into more massive nodes. The significant difference seen in the velocity distributions between the high- and low-redshift samples may conceivably reflect actual peculiar deceleration, the differences in spatial scale, or our selecting higher densities at lower redshift for a given detection threshold for Lyα forest lines.

We also investigate the alternative possibility that the velocity structure of the general Lyα forest could have an entirely different, local origin, as expected if the Lyα forest were produced or at least significantly modified by galactic feedback, e.g., winds from star-forming galaxies at high redshift. However, we find no evidence that the observed distribution of velocity shear is significantly influenced by processes other than Hubble expansion and gravitational instability. To avoid overly disturbing the IGM, galactic winds may be old and/or limp by the time we observe them in the Lyα forest, or they may occupy only an insignificant volume fraction of the IGM. We briefly discuss the observational evidence usually presented in favor of an IGM afflicted by high-redshift extragalactic superwinds and find much of it ambiguous. During the hierarchical buildup of structure, galaxies are expected to spill parts of their interstellar medium and to heat and stir the IGM in ways that make it hard to disentangle this gravitational process from the effects of winds.

Subject headings: cosmology: observations — gravitational lensing — intergalactic medium — quasars: absorption lines — quasars: individual (Q1422+2309, Q1424+2255, Q2345+007A, Q2345+007B, RX J0911+0551, SDSSp J143951.60−003429.2, SDSSp J143952.58−003359.2)

1. INTRODUCTION

Over the past decade our understanding of the general intergalactic medium (IGM), the main baryonic component of the cosmic web, has advanced considerably. Qualitative questions concerning the nature and interpretation of the IGM have given way increasingly to quantitative investigations aimed at measuring astrophysical properties of the general baryon field, among them the temperature, metallicity, kinematics, radiation field, and dependence on the underlying cosmological parameters. More and more we are able to obtain distributions of the astrophysical quantities as functions of time, spatial scale, and density, as opposed to mere mean values.

[1] Part of the observations were made at the W. M. Keck Observatory, which is operated as a scientific partnership between the California Institute of Technology and the University of California; it was made possible by the generous support of the W. M. Keck Foundation.

[2] Based partly on observations collected at the European Southern Observatory, Paranal, Chile (ESO programs 67.A-0371[A] and 69.A-0555[A]).

[3] Carnegie Observatories, 813 Santa Barbara Street, Pasadena, CA 91101.

[4] Astronomy Department, California Institute of Technology, Pasadena, CA 91125.

[5] Institute of Astronomy, Madingley Road, Cambridge CB3 0HA, UK.

[6] European Southern Observatory, Casilla 19001, Alonso de Cordova 3107, Santiago, Chile.

[7] Research Associate, Fonds National de Recherche Scientifique, Belgium.

[8] Massachusetts Institute of Technology, Center for Space Research, 77 Massachusetts Avenue, 37-664B, Cambridge, MA 02139.

Most studies on the large-scale properties of the IGM so far have concentrated on the crucial problem of the physical scale of Lyα forest clouds. The large sizes found (e.g., Weymann & Foltz 1983; Foltz et al. 1984; Smette et al. 1992, 1995; Bechtold et al. 1994; Dinshaw et al. 1994, 1995; Fang et al. 1996; Crotts & Fang 1998; Petitjean et al. 1998; Monier et al. 1999; Lopez et al. 2000; D'Odorico et al. 1998, 2002; Williger et al. 2000; Young et al. 2001; Aracil et al. 2002; Becker et al. 2004) have led to the realization that these clouds are really part of the general large-scale structure. Ionization arguments (Rauch & Haehnelt 1995), analytical and Monte Carlo modeling of absorption in double lines of sight (Smette et al. 1992, 1995; Charlton et al. 1995; Fang et al. 1996; Crotts & Fang 1998; Viel et al. 2002), and cosmological hydrodynamic simulations (Cen et al. 1994; Petitjean et al. 1995; Zhang et al. 1995; Hernquist et al. 1996; Miralda-Escudé et al. 1996; Wadsley & Bond 1997; Charlton et al. 1997; Cen & Simcoe 1997) all suggest that the absorbing structures are part of a filamentary cosmic web undergoing general Hubble expansion, at least in an average sense.

In the present paper we argue that the observations of the velocity field in the Lyα forest give us insights into the earliest stages of structure formation, when overdense regions break away from the Hubble flow and begin to collapse under the influence of gravity.

We address the question as to how the gaseous cosmic web actually expands, as a function of size, redshift, and density. We may reasonably expect that the cosmic web should follow the Hubble flow on large (Mpc) scales, i.e., at least on scales larger than the typical coherence length of these structures. On intermediate scales (of order 100 kpc) the effects of gravitational collapse may become more pronounced, and galactic and subgalactic potential wells may impart kinetic energy to the gas, whereas on the smallest (subkiloparsec) scales stellar evolution and gasdynamical processes in the interstellar medium (ISM; supernova remnants, winds) must be the dominant sources of kinetic energy and momentum. Earlier observations of small-scale structure in Lyα forest systems have shown (Rauch et al. 1999; 2001a, 2001b) that there is also a trend of the motions to increase in strength with increasing density; e.g., the higher density gas appears to be more turbulent than the more typical Lyα forest cloud.

To study the velocity field of the IGM we exploit the fact that an anisotropic, randomly oriented, expanding gas cloud will cause absorption features in two adjacent lines of sight intersecting it that are shifted relative to each other in proportion to the expansion velocity. Such shifts can be caused not only by the Hubble flow or gravitational collapse but by a wide range of other processes including galactic feedback and systematic rotation. Here we attempt to understand the origin of the observed motions.

The paper is structured as follows. The observations and data analysis are described in § 2, followed in § 3 by an analysis of the velocity differences between common absorption systems at the smallest ($\sim$1 kpc proper) scales as represented by the typical transverse separations between the beams to the gravitationally lensed QSO RXJ0911.4+0551 ($z = 2.79$; Bade et al. 1997). The cross-correlation function between the two Lyα forest sight lines is derived, and an alternative method is presented that measures the difference between the line-of-sight velocities of individual, manually selected absorption systems common to two adjacent sight lines. The resultant distribution of velocity differences for RX J0911.4+055 is discussed. Section 4 presents the same analysis at larger scales from 60 to about 300 h_{70}^{-1} kpc

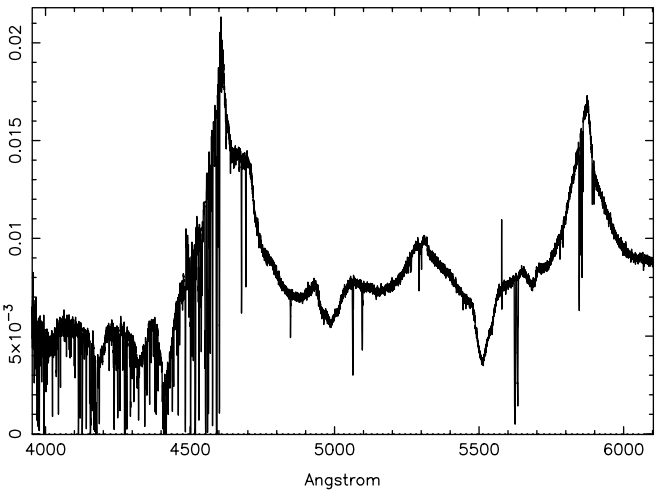

FIG. 1.—ESI spectrum of RX J0911.4+0551AB. Note the broad absorption troughs. The flux is in arbitrary units.

using the information from the QSO pairs Q2345+007AB ($z = 2.16$; Weedman et al. 1982), Q1422+2309A (Patnaik et al. 1992) and Q1424+2255 ($z = 3.63$; Adelberger et al. 2003), and SDSSp J143952.58−003359.2 and SDSSp J143951.60−003429.2 (hereafter abbreviated as Q1439−0034AB; $z = 4.25$; Schneider et al. 2000). The interpretation of the observed distribution is given first in light of a simple analytic model where the Lyα clouds are randomly oriented expanding pancakes of gas, in a discussion similar to Haehnelt (1996) and Charlton et al. (1995, 1997). A further comparison is made with fake Lyα forest spectra from a cosmological hydrodynamic simulation (Viel et al. 2004), which is analyzed for velocity differences among absorbers in exactly the same way as the real data. Noting the excellent agreement for the distributions of velocity shear between data and simulation, we proceed to study and interpret the distribution of expansion velocities for absorbing clouds in the simulation. Section 5 on the possible influence of "cosmological superwinds" on the kinematics of the IGM precedes the final discussion and summary.

2. OBSERVATIONS AND DATA ANALYSIS OF MULTIPLE LINES OF SIGHT

2.1. *RX J0911.4+0551*

RX J0911.4+0551 is a radio-quiet $z = 2.79$ QSO. This object was identified as a gravitationally lensed quasar by Bade et al. (1997). The image configuration consists of four images in an "animal paw" pattern with mutual separations of up to 3.″1 (Burud et al. 1998). The object appears to be lensed by a galaxy cluster at $z = 0.7689$ (Burud et al. 1998; Kneib et al. 2000). The QSO itself is a mini–broad absorption line (BAL) QSO (Bade et al. 1997); in the present data (see below) we detect triangular troughs at blueshifts of 18,700 km s^{-1} relative to the QSO's broad C IV emission peak (Fig. 1). The absorption troughs are visible at $z = 2.559$ in the transitions H I λ1216, N V $\lambda\lambda$1239, 1243, C IV $\lambda\lambda$1548, 1551, Si IV $\lambda\lambda$1393, 1403, and Al III $\lambda\lambda$1855, 1863. There is another weaker trough at 5683 Å, probably another C IV component blueshifted by 10,000 km s^{-1}.

We observed the lensed images with the Keck II Echelle Spectrograph and Imager (ESI; Sheinis et al. 2002) on 2000 March 3 and 4 for 3600 s (A images) and 10,800 s (B image). The spectra were taken with a 0.″75 wide and 20″ long slit

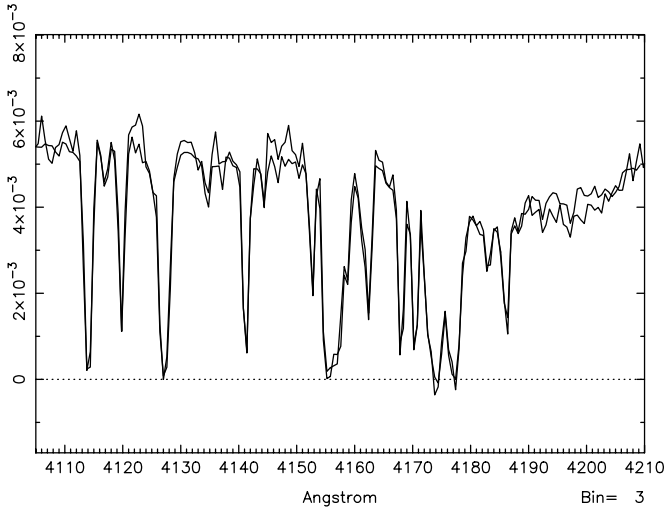

FIG. 2.—Raw section of the spectra of RX J0911.4+0551AB prior to flux calibration and continuum fitting. The flux is in arbitrary units. The figure shows that the similarities between the Lyα forests are not artifacts of the data reduction.

leading to a spectral resolution of 48.9 km s^{-1} near the center of the spectrum. The slit was placed on the sky at a fixed position angle of 10°.

Our results are based on a comparison between the spectra of a spatial average of images A1, A2, and A3 on one hand and image B on the other (in the nomenclature for the lensed images established by Burud et al. 1998). The B image was always well separated from the others, but because of the small separation between the A images, it was not possible to resolve them separately and components A1, A2, and A3 were partly on the slit simultaneously. We assume a nominal separation of 3.″1 between the combined "A image" and B, and below we refer to spectra A and B only, but one should keep in mind that the A spectrum is a spatial average.

The data were extracted, wavelength-calibrated, and fluxed using the custom data reduction package MAKEE[9] (Barlow & Sargent 1997). The signal-to-noise ratios (S/Ns) in the Lyα forest region at 4260 Å at the continuum level are 56 and 27 per 3 pixel resolution element for the A and B images, respectively.

To compare the absorption features between the different spectra, the overall shape of the spectra has to be matched. The IRAF continuum task was used to fit a multiknot spline3 curve to the ratio of the A and B spectra, ignoring spectral regions obviously affected by absorption lines. The density of knots ranged from one degree of freedom per 400 km s^{-1} near the H I Lyβ emission line to one per 340 km s^{-1} near the H I Lyα line. This approach wipes out genuine differences between the spectra on large velocity scales but preserves differences between individual absorption lines on scales smaller than a few hundred km s^{-1}. It also takes out the BAL troughs. To illustrate that the lack of differences between the spectra is not due mainly to an overly flexible continuum fit, we show in Figure 2 a section of the two spectra (on top of each other) *before* any continuum fitting is done. The mean proper transverse separations between the lines of sight here is 1.1 h_{70}^{-1} kpc. The spectra have only been scaled globally to take out the overall difference in flux between the images. The similarity is remarkable, and there are few obvious differences in line strength and position for most individual absorption lines. The section of the spectrum shown includes part of one of the BAL troughs; there are some significant larger scale variations between 4190 and 4210 Å at low optical depths that are probably caused by structure in the BAL outflow.

In any case, it is clear just from visual inspection that the IGM is highly homogeneous on kiloparsec scales. Any differences in column density and or velocity across the lines of sight must be subtle.

The following sections describe various ways of quantifying this result.

2.2. *Q2345+007AB*

This object, long suspected of being a gravitationally lensed QSO, has recently been shown (A. Smette et al. 2005, in preparation) to be a genuine QSO pair. The data were obtained with the UVES instrument on the ESO VLT. A total of 18,600 s over three exposures was obtained for image A and 60,000 s over nine exposures for image B. All observations were carried out in service mode between 2001 July 25 and 2002 October 6, usually with seeing conditions better than 0.″8. The slit was aligned along the parallactic angle to reduce slit loss to a minimum. No ADC (atmospheric dispersion corrector) was used. The data reduction is described in A. Smette et al. (2005, in preparation).

2.3. *Q1422+2309A/Q1424+2255 and Q1439−0034AB*

The data and their reduction and a global correlation analysis of their Lyα forests are described in Becker et al. (2004). For the comparison between Q1422+2309 and Q1424+2255 only the spectrum of the A image of Q1422+2309 was used.

2.4. *Contamination of the Lyα Forest by Metal Absorption Systems*

QSO metal absorption systems strong enough to be visible in spectra of the current data quality (S/N $\sim$ 10−70) are usually associated with strong, mostly saturated Lyα forest lines. As shown in previous papers (e.g., Rauch et al. 2001a), such "strong" metal absorbers almost invariably show structure (velocity, column density changes) over a few hundred parsecs. Thus, if the metal transition lines are mistaken for H I Lyα lines, the turbulence of the IGM will be overestimated and the correlation length of the IGM underestimated. We have inspected the wavelength stretches in the Lyα forest region potentially affected by transitions belonging to metal absorbers identified from other transitions redward of the Lyα line belonging to the same system. Where the contamination was deemed significant these regions were omitted from the analysis. Given our moderate S/Ns and resolution it is inevitable that some metal absorption systems are being missed, especially if they have only lines embedded in the Lyα forest.

3. SEARCHES FOR STRUCTURE IN THE Lyα FOREST ON KILOPARSEC SCALES

This section discusses two methods to quantify differences between Lyα forest spectra from adjacent lines of sight: the cross-correlation function as a measure of *global* differences (§ 3.1), and the comparison of the velocities of *individual* absorption systems between the sight lines (§ 3.2).

3.1. *Global Differences between the Spectra*

As in Rauch et al. (2001b) and Becker et al. (2004), we can study global differences in the Lyα forest region by measuring the cross-correlation function ξ_{cc} over the total usable length of both spectra (see below).

[9] See http://spider.ipac.caltech.edu/staff/tab/makee/index.html.

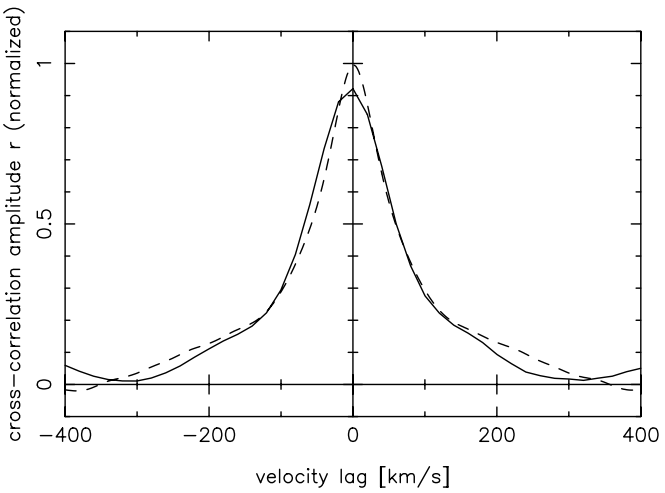

FIG. 3.—Cross-correlation function $r(\langle d\rangle, \Delta v)$ for a mean beam separation $\langle d\rangle = 1.0\ h_{70}^{-1}$ kpc between the Lyα forests in RX J0911.04+0551AB (*solid line*). For comparison, the same function is shown for the closer separation ($\langle d\rangle = 0.108\ h_{70}^{-1}$ kpc) Q1422+231AC image pair (*dashed line*). The peak for the RX J0911 case is slightly shifted to the left because of uncertainties in the placement of the images on the spectrograph slit (see text).

We define this quantity again by

$$\xi_{\rm cc}(\Delta v, \Delta r) \equiv \frac{\langle [F_r(v) - \langle F_r\rangle][F_{r+\Delta r}(v+\Delta v) - \langle F_{r+\Delta r}\rangle]\rangle}{\sqrt{\left\langle [F_r(v) - \langle F_r\rangle]^2\right\rangle \left\langle [F_{r+\Delta r}(v+\Delta v) - \langle F_{r+\Delta r}\rangle]^2\right\rangle}}. \quad (1)$$

The quantities F_r and $F_{r+\Delta r}$ are the pixel flux values of the two spectra, separated by Δr on the plane of the sky. The velocity coordinate along the line of sight is v (where $dv = d\lambda/\lambda$), and Δv is the velocity lag. The averages are taken over most of the velocity extent of the spectrum. For $\Delta r = 0$ we get the usual autocorrelation function $\xi_{\rm cc}(\Delta v, 0)$, while for $\Delta v = 0$ we have the cross-correlation as a function of transverse separation[10] only. The function is defined so as to satisfy $\xi_{\rm cc}(0,\ 0) = 1$. With large-scale velocity correlations (>1000 km s^{-1}) expected to be absent or weak (Sargent et al. 1980), the autocorrelation function (on scales of $\sim$100 km s^{-1}) mostly measures the Lyα line width and the weak small-scale clustering of Lyα forest systems (e.g., Webb 1987; Rauch et al. 1992). We apply the correlation analysis to the wavelength interval [3950, 4614] Å of the QSO in our sample with the smallest separation between its images, RX J0911.4+0551A and B. Thus most of the spectral region between Lyβ and Lyα emission is included, omitting only a small region [4381, 4386] Å where there is a significant contamination by a known metal Si III λ1206 interloper at $z = 2.633$. The resulting mean redshift $\bar{z} = 2.522$ of the remaining sample corresponds to a mean beam separation[11] $\overline{\Delta r} = 1.0\ h_{70}^{-1}$ kpc.

The function $\xi_{\rm cc}(\Delta v, \overline{\Delta r})$ is shown in Figure 3. In particular, we obtain the "zero lag" cross-correlation function for the RX J0911.4+0051 lines of sight:

$$\xi_{\rm cc}\left(\Delta v = 0,\ \overline{\Delta r} = 1.0\ h_{70}^{-1}\ {\rm kpc}\right) = 92.1\%. \quad (2)$$

[10] Throughout this paper beam separations are computed for a flat universe with $\Omega_m = 0.25$ and $h_{70} = 1$. In our earlier papers beam separations were given for a $\Omega_m = 1.0$, $h_{50} = 1$ cosmology, but the values differ by less than 20% between the cosmological models for the redshift range considered here.

[11] The redshift of the lens of RX J0911.4+055 is taken to be $z = 0.7689$ (Kneib et al. 2000).

For comparison, the dashed line shows the same quantity for the pair of sight lines between the Q1422+231 images investigated in Rauch et al. (2001b). The mean separation there is about an order of magnitude smaller:

$$\xi_{\rm cc}\left(\Delta v = 0,\ \overline{\Delta r} = 108\ h_{70}^{-1}\ {\rm pc}\right) = 99.5\%. \quad (3)$$

Thus, even at the larger kiloparsec separation probed with the new, RX J0911.4+0551 data, the global differences between the spectra are very small, indicating that the average coherence length in the IGM is much larger than a kiloparsec.

3.2. *Local Differences: Velocity Shear in Individual Absorption Systems*

The above correlation analysis has only shown that the cosmic web *on average* is highly coherent on kiloparsec scales. Nevertheless, infrequent but strong local differences in column density as well as velocity shifts (caused by galactic winds, rotation, or any small-scale structure in the ISM of an intersected galaxy) could easily manifest themselves on scales of a few hundred km s^{-1} without degrading the cross-correlation signal significantly.

To investigate this possibility and to get a more quantitative understanding of what is happening at the level of a single absorbing cloud, we have searched for velocity shifts among *individual* absorption lines or small complexes between the two lines of sight. We had attacked this question previously in Rauch et al. (2001b), where the Lyα forest lines in Q1422+231 had been modeled with Voigt profiles. The decomposition into multiple Voigt profiles becomes more ambiguous at the lower (ESI) spectral resolution available here, which makes the pairwise comparison between components in separate lines of sight less certain.

Thus, in the present case a different, less model-dependent method was adopted. Individual absorption lines are selected by eye, by marking a wavelength window including the line with a cursor. It was generally attempted to delineate the absorption lines by marking the points on either side of the line center where the continuum had substantially recovered, but this approach was not always possible and sometimes a much closer section around the line center had to be chosen to avoid contributions from a blended component with seemingly different kinematics. However, the measurement should not be very sensitive to the exact width and position of the window, as this is a relative measurement and it is only important that the same window be imposed on both spectra. This is repeated for all lines deemed to be H I Lyα. Then the difference between the flux-weighted projected velocities, or the *velocity shear*, $\Delta\overline{v} = \overline{v_{\rm B}} - \overline{v_{\rm A}}$, is computed for each window along the lines of sight A and B, where the velocity weighted by the absorbed flux is defined as

$$\overline{v} = \frac{\sum_i w_i v_i}{\sum_j w_j}. \quad (4)$$

Here the flux weight w_i of a pixel i is $w_i = (1 - f_i)$, with f_i being the flux relative to a unit continuum, and the summation is over all pixels of the chosen spectral window enclosing the absorption line. The width of the pixels is constant in velocity space. The origin of the velocity coordinate is defined to be the center of the window around the absorber. The absorption regions of the spectrum included in the analysis are shown as blackened areas in Figure 4.

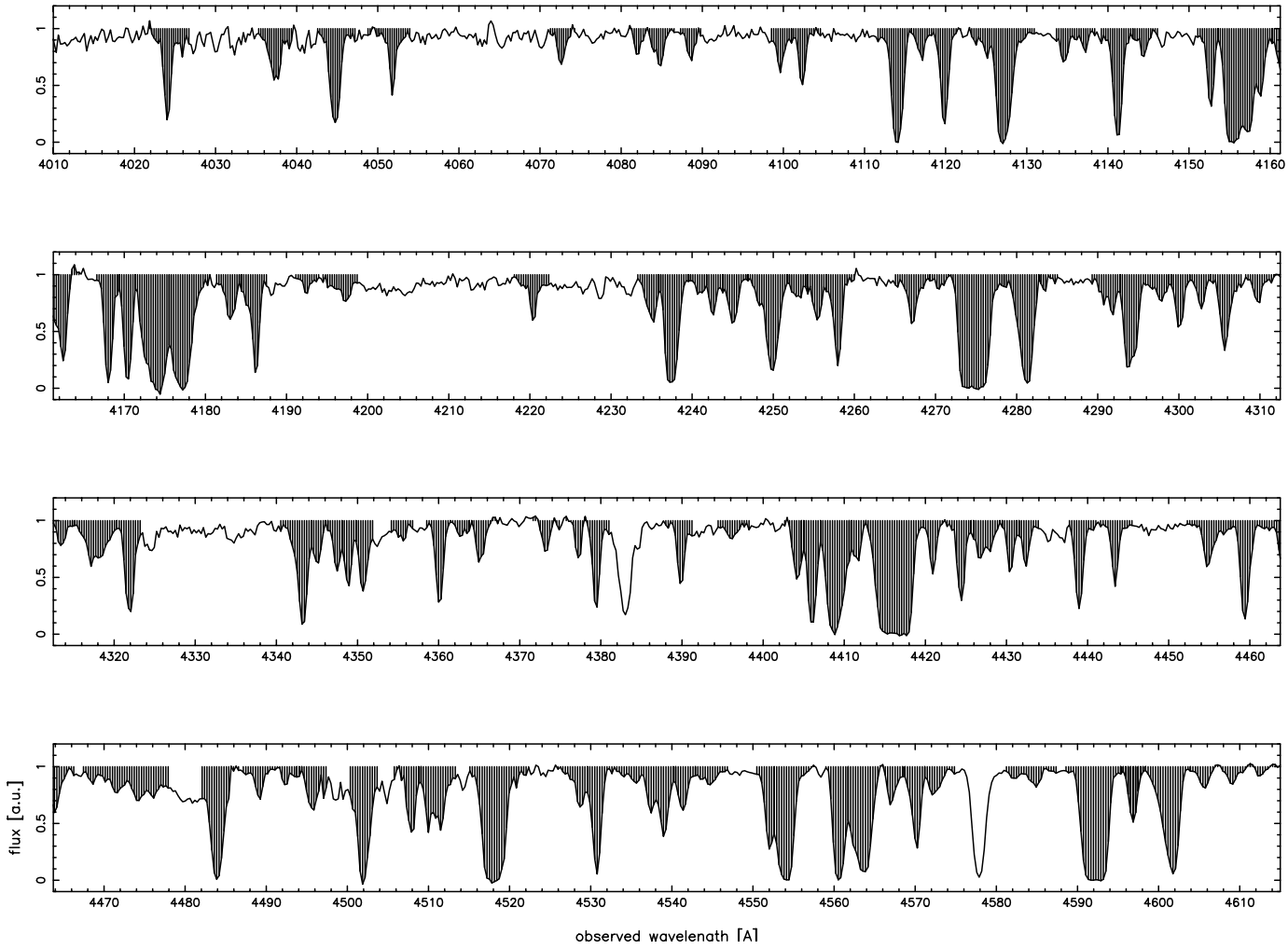

FIG. 4.—Lyα forest spectrum of RX J0911.04+0551A with the filled parts indicating the regions used for the measurement of the velocity differences. The omitted regions were either deemed to depart too little from the continuum or were affected by metal-line interlopers.

To see whether there are intrinsic velocity shifts $\Delta\overline{v}$ between the lines of sight exceeding the scatter due to measurement uncertainties, the variance in the velocity measurement needs to be computed.

The variance in the determination of $\overline{v}$ from equation (4) is then

$$\sigma^2(\overline{v}) = \frac{\sum_i v_i^2 \sigma^2(w_i)}{\left(\sum_j w_j\right)^2} + \frac{\left(\sum_k w_k v_k\right)^2 \sum_i \sigma^2(w_i)}{\left(\sum_j w_j\right)^4}, \qquad (5)$$

where $\sigma(w_i)$ is the standard deviation of the normalized absorbed flux of pixel i. This is just the error of the flux in that pixel as derived from the original error array, based on photon counting statistics. There is no term accounting for the error in the velocity calibration, which we assume to be negligible for the time being. The variance in the velocity difference is simply

$$\sigma^2(\Delta\overline{v}) = \sigma^2(\overline{v_{\rm B}}) + \sigma^2(\overline{v_{\rm A}}). \qquad (6)$$

The distribution of the observed differences in projected velocities between the lines of sight, $\Delta\overline{v}$, is shown in Figure 5. The data are taken from 108 absorption regions spanning 4000–4614 Å, i.e., from Lyα not quite down to Lyβ (a noisy bit at the

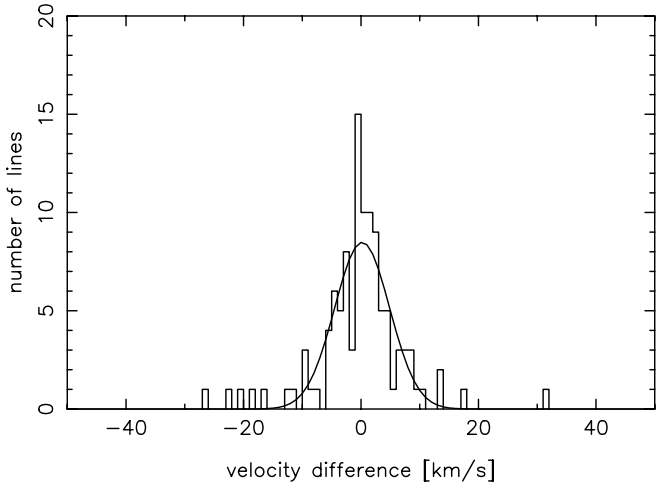

FIG. 5.—Observed histogram of the velocity differences Δv (= $v_{\rm B} - v_{\rm A}$) for pairs of absorption components toward RX J0911.04+0551AB. The solid curve is the expected Gaussian distribution, if the width were entirely caused by the mean measurement error $\sigma(v_{\rm B} - v_{\rm A}) = 4.7$ km s^{-1} and there were no intrinsic differences between the lines of sight. There are a few outliers with 3 σ significant velocity differences that are shown individually in Fig. 6.

low-wavelength end below 4000 Å was left out). Lyα lines in four other regions were left out because of blends with metal-line interlopers from an absorption system at higher redshift: regions 4383–4386 Å and 4323–4339 Å were affected by blends with the Si III λ1207 and Si II $\lambda\lambda$1190, 1193 lines, respectively, from a system at $z = 2.6327$. Similarly, the Lyα line near 4577.9 Å is blended with Si II λ1260 from the same absorber.

The mean velocity shift between the lines of sight, obtained from the average of all velocity shifts of all remaining 108 regions, weighted by the inverse of the square of the measurement error, was found to be 1.63 ± 0.17 km s^{-1}. Such a shift has been seen before between lensed spectra of QSOs (Rauch et al. 2001b) and is most likely caused by the uncertainty involved in placing both images (sequentially) at the same position on the spectrograph slit. When comparing the actual distribution of the velocity differences with the one predicted by observational scatter, the mean shift was subtracted first. The 108 lines are at mean redshift 2.567, corresponding to a transverse separation of 0.82 h_{70}^{-1} kpc between the beams.

The *observed* absolute value of the velocity difference, averaged over all regions, amounts to

$$\langle |\Delta \bar{v}| \rangle = 4.9 \text{ km s}^{-1}. \quad (7)$$

The observed rms velocity difference is

$$\sqrt{\langle \Delta^2 \bar{v} \rangle} = 7.4 \text{ km s}^{-1}, \quad (8)$$

whereas the standard deviation for the velocity differences predicted on the basis of the measurement errors alone is

$$\sigma(\Delta \bar{v}) = 4.7 \text{ km s}^{-1}. \quad (9)$$

A χ^2 test shows that the innermost ± 13 km s^{-1} (equivalent to 2.8 σ) of the observed distribution of projected velocity differences between the lines of sight, $\Delta \bar{v}$, has a 40% probability of having been drawn from a Gaussian error distribution with $\sigma(\Delta \bar{v}) = 4.7$ km s^{-1} (Fig. 5); i.e., most of the velocity differences are consistent with pure measurement error.

However, there are hints of some significant excursions beyond mere measurement uncertainty. Of the observed velocity differences, 37% exceed 1 σ if predicted by the measurement error, and 4.6% (five systems) are beyond 3 σ (eq. [6]). Note that the excursions here are with respect to the individual measurement uncertainty for a particular region, which generally is different from the width of the distribution (eq. [9]).

The 10 cases of absorption lines with larger than 2.5 σ velocity shifts are shown in Figure 6. Perhaps half of them are borderline cases where a bad continuum fit or some defect in one spectrum could have produced an artifact. None of the remaining systems exhibit any unusual evidence for strong turbulence or strong column density gradients, but they appear to be consistent with a mere *velocity shift of the entire absorption system*. The mean absolute shift in these 10 cases is 11 km s^{-1}.

Subtracting in the above cases the predicted width of the distribution based on errors alone from the measured rms width in quadrature, we need to explain an additional width of about 6 km s^{-1} rms as having a physical origin. We can only speculate about the origin of these shifts. The Hubble expansion over kiloparsec distances like the ones considered here would only cause immeasurably small velocity gradients. The most likely explanation appears to be the presence of a nearby gravitational potential well (associated with the grainy mass distribution in the filaments) in which the gas is "circling the drain," i.e., undergoing rotation or differential motion during gravitational infall.

4. THE TRANSITION TO LARGER SCALES

With increasing transverse separation between the lines of sight, absorption systems become increasingly decoherent, as can be seen from a comparison of sections of the spectra of RX J0911.4+055, Q2345+007AB, and Q1422+2309A/Q1424+2255 (Fig. 7). The figure shows three sections of the QSO lines of sight chosen to have equal comoving extent of 100 h^{-1} Mpc. The spectra along the two lines of sight to two different QSO images in each panel are represented by a thick line and a thin line. The spectra to RX J0911.4+055 are essentially identical in both lines of sight over a mean transverse separation of 0.22 h_{70}^{-1} physical kpc. Aside from the obvious differences in S/N and mean absorption (note the different redshifts between the panels), the most obvious change when going from the top to the bottom panel is the increasing dissimilarity between the spectral pairs.

The Q2345+007AB spectra at a mean separation of 60.7 h_{70}^{-1} proper kpc already differ somewhat in the column densities and positions of individual lines, but all of the systems can still easily be cross-identified among the lines of sight. For the case of Q1422+2309A/Q1424+2255 shown here (from Becker et al. 2004), at a mean separation of 285 h_{70}^{-1} kpc there are strong differences for individual systems, which often cannot be traced easily across the lines of sight. Nevertheless, voids (regions of low absorption) and strong lines can still be recognized reasonably often across the lines of sight if one allows for some shifts in the projected velocity and for column density differences.

Clearly there are scales where the observed velocity shear (i.e., the differences between the velocities projected along the line of sight of two absorption lines observed in adjacent lines of sight) must be dominated by the underlying systematic expansion of the cosmic web. With the exception of the case of RX J0911.4+055, the beam separations for the QSOs considered here are large enough that a significant amount of the velocity shifts between individual absorption lines across the lines of sight should arise in the Hubble flow.

4.1. *The Observed Distribution of Velocity Shear*

The transition to larger scales dominated by the Hubble flow should be visible as a change in shape of the distribution function of velocity shear. For the wider separation pairs the flux-width weighted velocity differences between the lines of sight were measured as before, for individual absorption systems in regions selected by eye. A uniform minimum rest-frame equivalent width of 0.4 Å was required as a necessary but not sufficient condition for all lines in order to be included in the samples. Because of the wider separations not all systems could be successfully cross-identified. Doubtful cases, where the continuation of an absorption system across the sky was ambiguous, were omitted, leading us to err on the conservative side. Figures 8, 9, and 10 show again the selected regions as "blackened" and give an illustration of the severity of this selection effect. The observed distributions for the wider separation QSO pairs are shown as histograms in Figure 11 (for Q2345+007AB) and Figure 12 (where the velocity shear measurements of Q1422+2309A/Q1424+2255 and Q1439−0034AB have been combined into one histogram because the redshifts and separations are similar). The velocity shifts were determined in the same way as described for RX J0911.4+055 above.

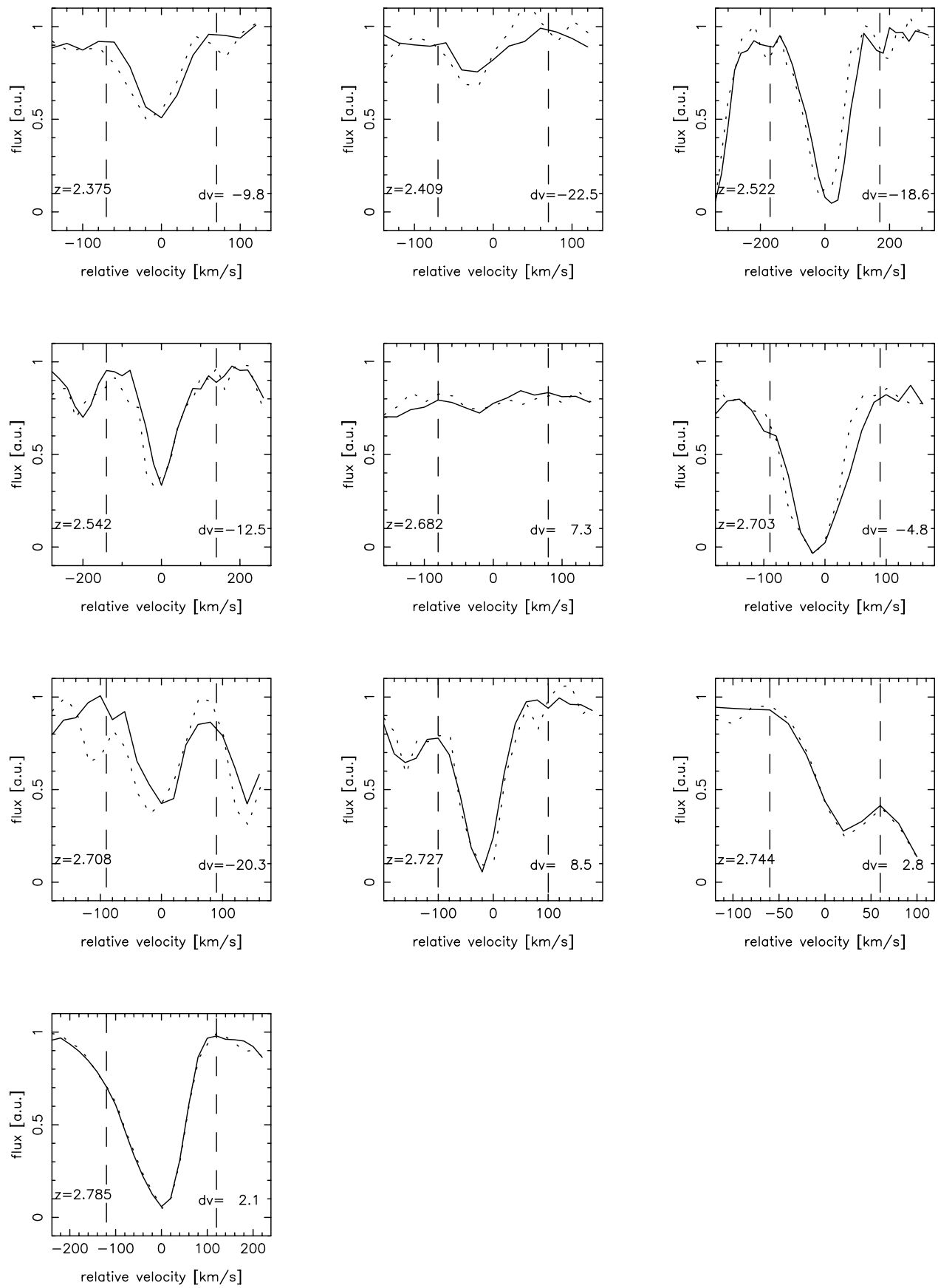

FIG. 6.—Absorption lines toward RX J0911.04+0551AB with velocity differences between the lines of sights larger than 2.5 σ. The differences between the spectra appear to be mostly consistent with velocity shifts of the entire absorption system. The measured velocity shifts *dv* are shown in each panel in units of km s^{-1}.

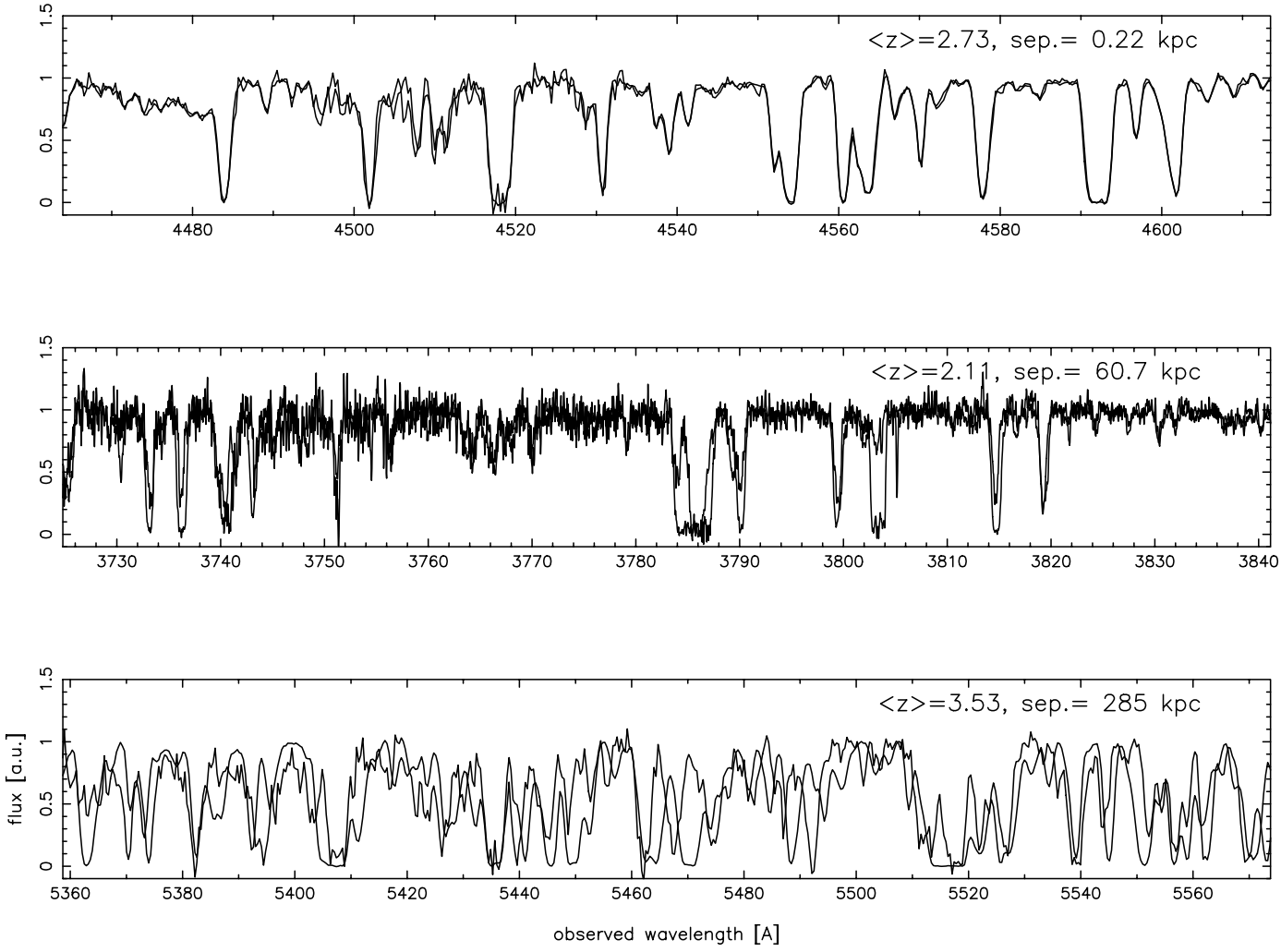

FIG. 7.—Sections of the three Lyα forest double lines of sight, in the order of increasing separation between the lines of sight (*top to bottom*: RX J0911.4+055, Q2345+007AB, Q1422+2309A/Q1424+2255). The length of the spectra is chosen in all cases to be 100 h^{-1} comoving Mpc. The mean redshifts and the mean beam separation (in physical h_{70}^{-1} kpc) are given in the upper right corner of the spectra. The discrepancies between the column densities and velocities of the individual absorption lines are generally insignificant for the case with subkiloparsec beam separation, but they become noticeable at 60 kpc and quite dramatic at 285 kpc. Note that even in the last case there still is quite a bit of similarity between the lines of sight.

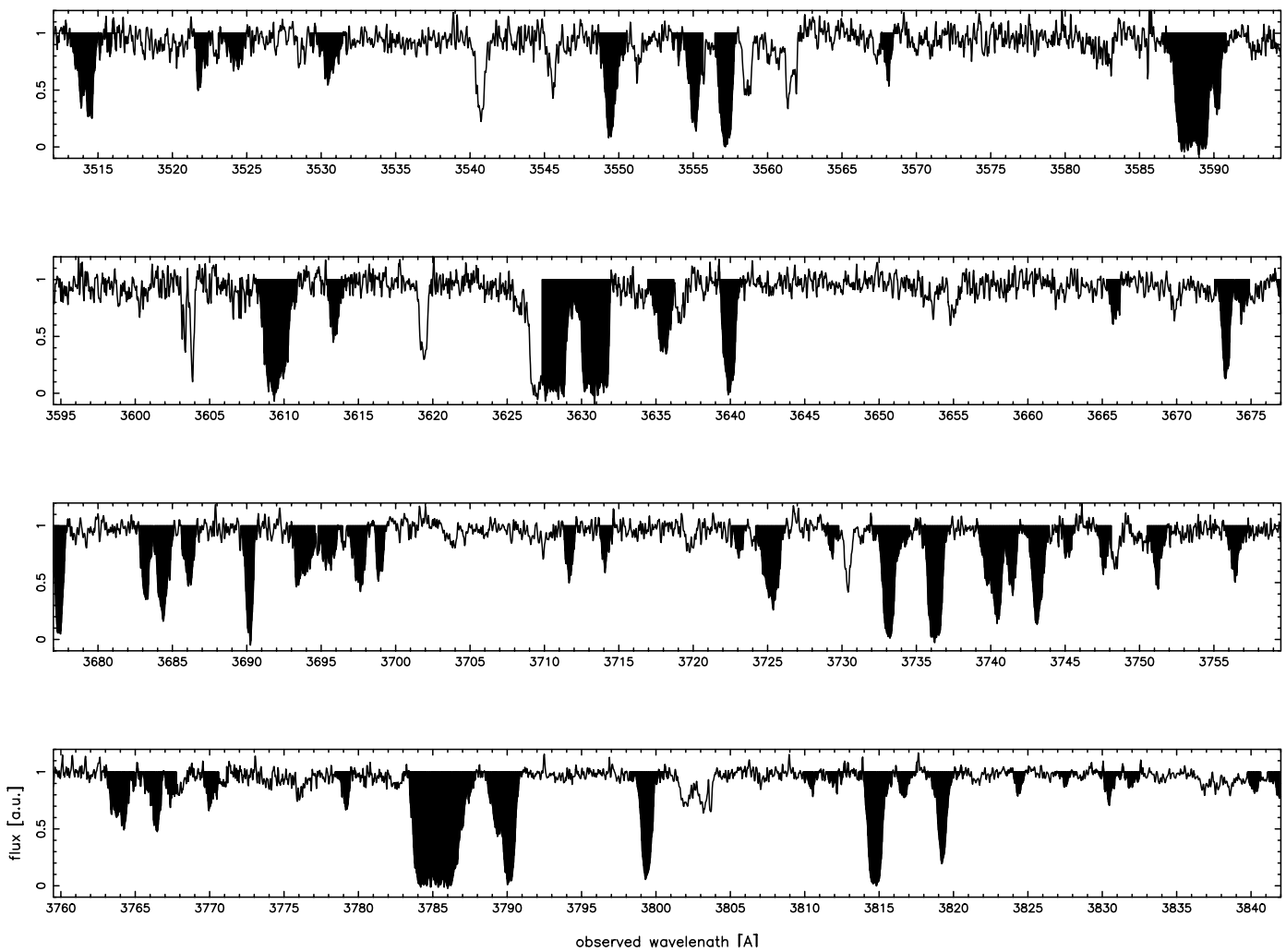

FIG. 8.—Lyα forest spectrum of Q2345+007AB, with the filled parts indicating the regions used for the measurement of the velocity differences. The omitted regions were either deemed to depart too little from the continuum or were affected by metal-line interlopers.

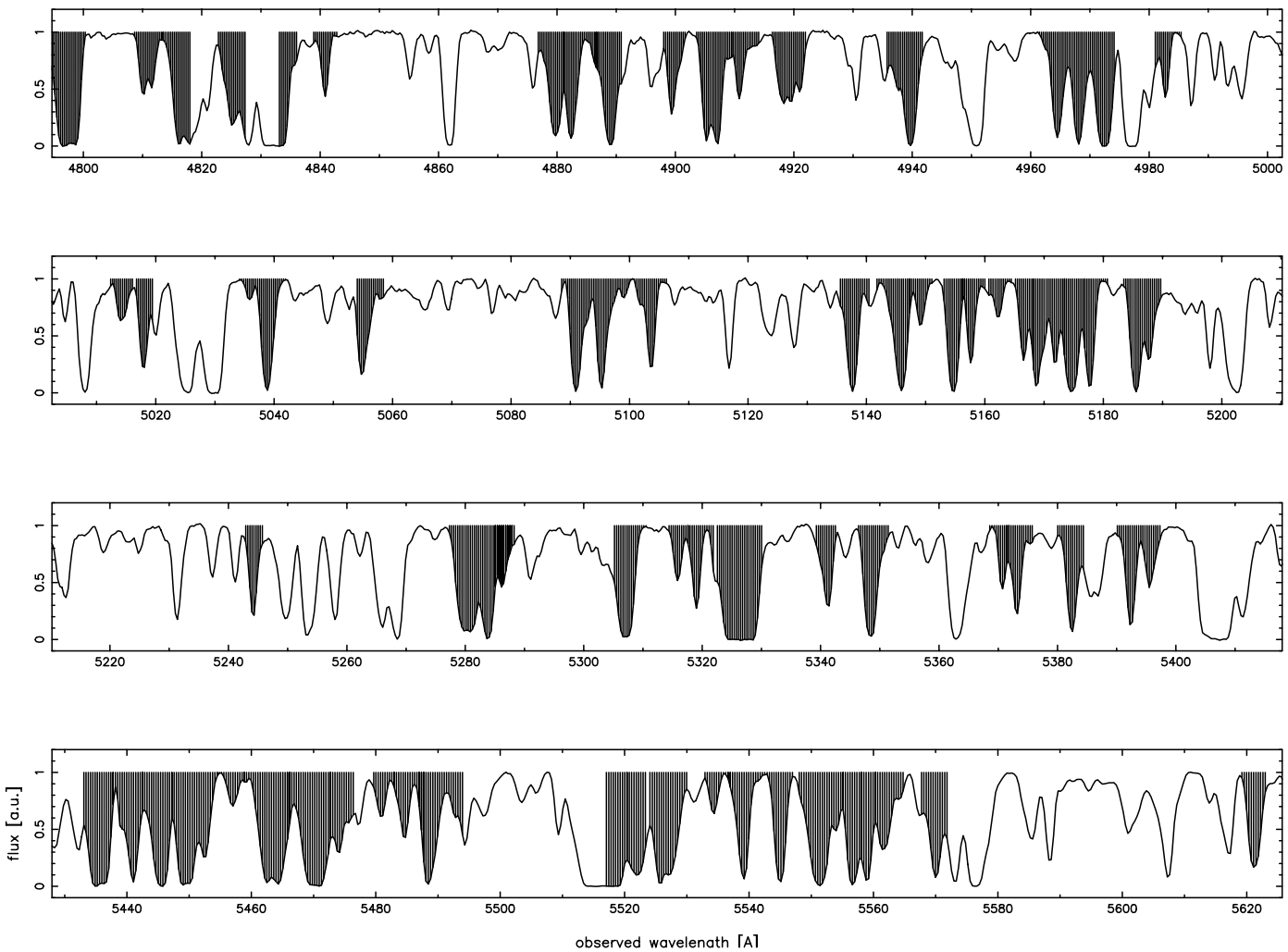

FIG. 9.—Lyα forest spectrum of Q1422+2309A/Q1424+2255, with the filled parts indicating the regions used for the measurement of the velocity differences.

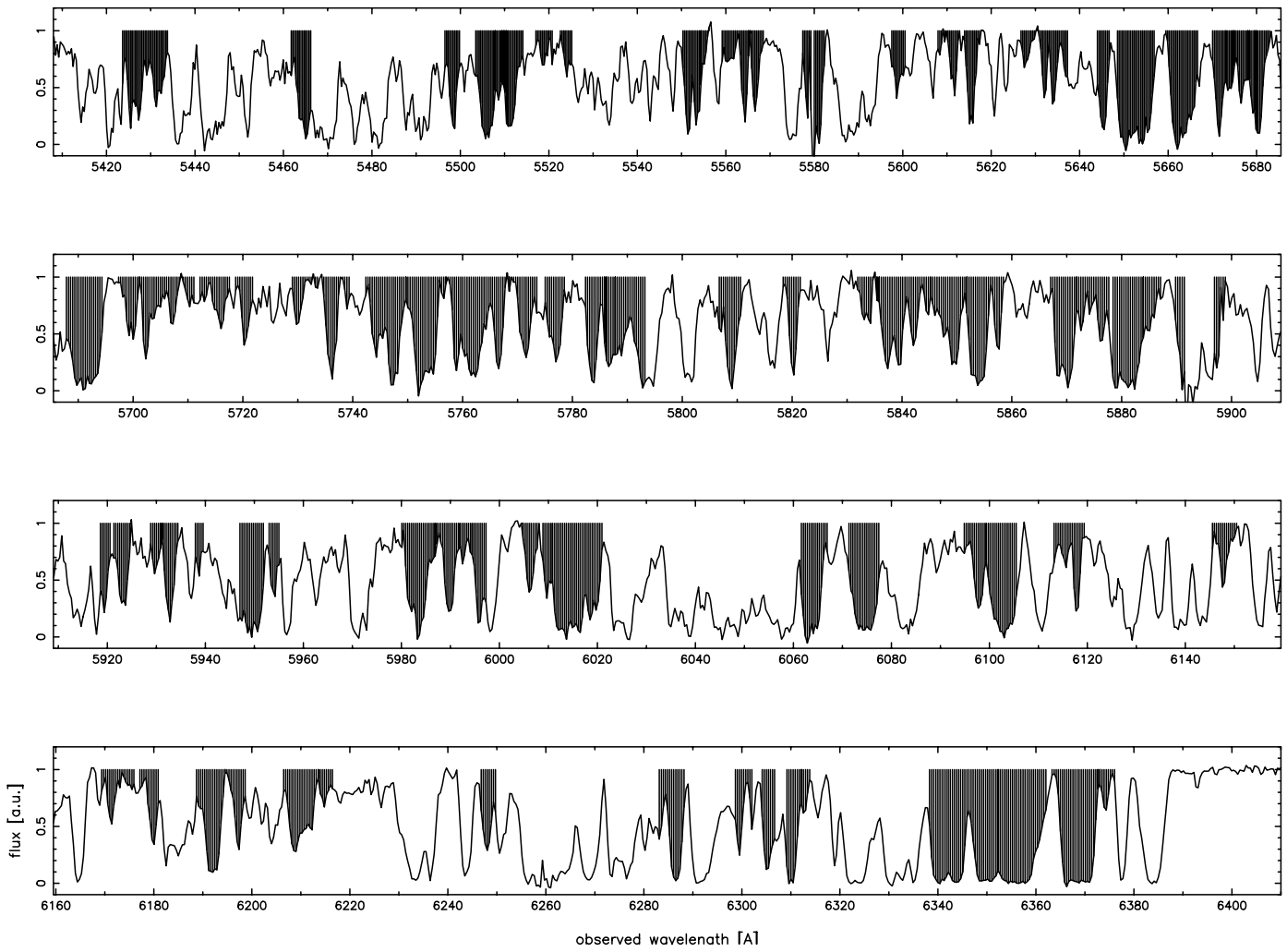

FIG. 10.—Same as Fig. 9, but for Q1439−0034AB.

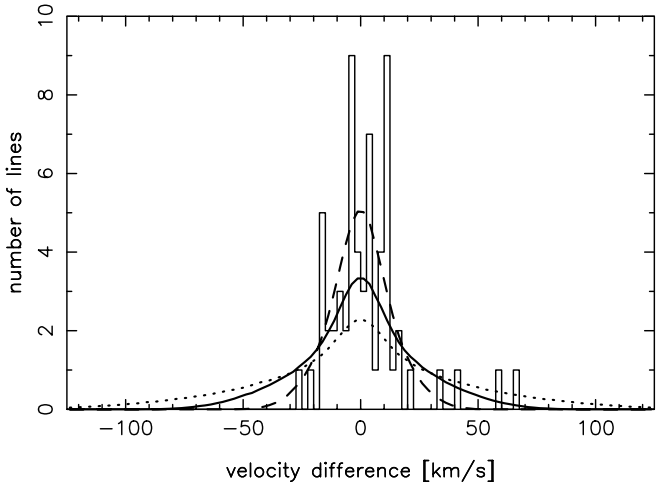

FIG. 11.—Velocity shear between the lines of sight for Lyα forest lines in the spectra of Q2345+005AB. The histogram gives the *observed* distribution of the measured shear between corresponding absorption lines in the two lines of sight. The solid line is the best-fit expanding pancake model with $v = 0.8 v_{\rm Hubble}$. For comparison, the dashed and dotted lines show the model distribution for $v = 0.4 v_{\rm Hubble}$ and $1.5 v_{\rm Hubble}$, respectively.

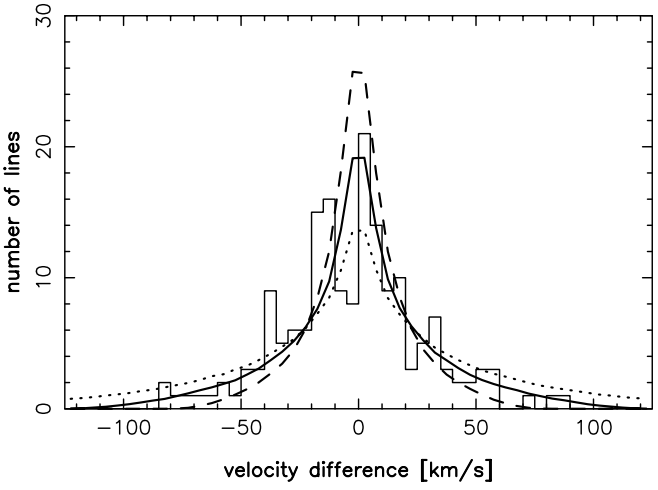

FIG. 12.—Velocity shear between the lines of sight for Lyα forest lines in the spectra of Q1439−0034AB and the pair Q1422+2309A/Q1424+2255. The histogram gives the combined *observed* distributions of the two pairs. The solid line is the best-fit expanding pancake model with $v = 0.65 v_{\rm Hubble}$. For comparison, the dashed and dotted lines show the distribution for $v = 0.4 v_{\rm Hubble}$ and $1.2 v_{\rm Hubble}$, respectively.

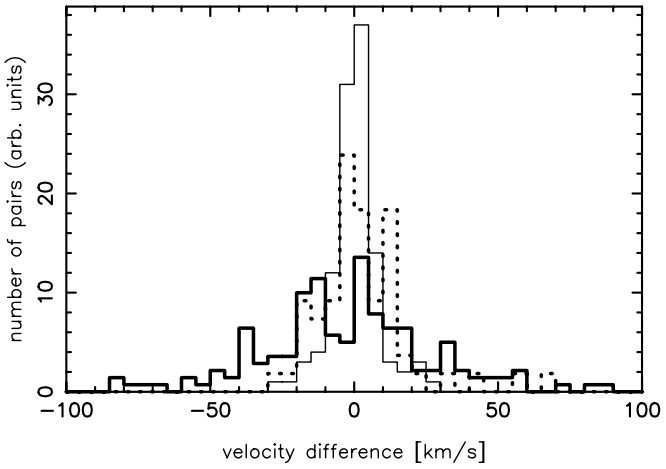

FIG. 13.—Observed distributions of velocity shear with the histograms from Figs. 5, 11, and 12 normalized to the same integral (arbitrary units) and overplotted on top of each other. The RX J0911.4+055 sample is represented by the thin-lined histogram, the Q2345+007AB sample by the dotted one, and the high-redshift combined Q1422+2309A/Q1424+2255 and Q1439−0034AB samples by a thick solid histogram.

Figure 13 shows all three observed shear distributions on the same velocity scale. Compared with the Gaussian scatter seen in the case of the very close lines of sight to RX J0911.4+055, the distributions for the velocity shear in Q2345+007AB at a separation of 60.7 kpc (Fig. 11) looks less Gaussian, and the combined distribution for the two higher redshift pairs (Fig. 12) (Q1422+2309A/Q1424+2255 and Q1439−0034AB) has clearly developed broad wings, not unlike a Lorentzian. Below we show that this peculiar shape is exactly what is expected for a population of randomly oriented, highly flattened structures expanding with the general cosmic web.

The distribution histograms as shown in Figures 11 and 12 are incomplete at a level that depends mainly on confusion as the absorption-line density goes up with redshift, and partly on the noisiness of the data. Confusion happens when two absorption lines in two adjacent lines of sight are mistakenly ascribed to the same underlying cloud. The rate of incidence per unit redshift of absorption lines around redshift 2 is still small enough that this is not a concern, but beyond redshift 3 the likely velocity shifts become comparable to the average redshift separation along the line of sight between absorption lines. Moreover, separations between the lines of sight on the order of several hundred kiloparsecs as considered here already exceed the typical length over which Lyα absorbers are uniform enough to merit speaking of individual clouds (Cen & Simcoe 1997). Then it is difficult to be sure that a given absorption system continues across the sky in the other line of sight. For the two high-redshift pairs discussed here and shown in Figure 12, the incompleteness is estimated to set in already at velocity differences of less than 100 km s^{-1}, leading to a systematic underestimate of the width of the velocity distribution. Below we describe how to correct for these systematic errors by analyzing simulated Lyα forest spectra from a cosmological simulation in exactly the same way as the real data, in an attempt to introduce the same biases and relate the observed width of the velocity shear distribution to the underlying three-dimensional kinematics of the gas.

4.2. *Modeling the Distribution of Velocity Shear as Large-Scale Expansion*

To get a qualitative understanding of the observed motions we first proceed to analytically model the observed shape of the distribution of velocity differences to see whether it is consistent with motions expected of clouds partaking in the Hubble expansion. Moreover, we check whether the order of magnitude of the expansion velocity is really consistent with this interpretation.

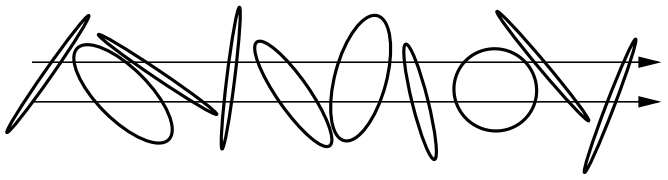

FIG. 14.—Randomly orientated, radially expanding pancakes intersecting two close lines of sight.

In the spirit of Haehnelt (1996) and Charlton et al. (1995, 1997) we start with a simple model of the expanding clouds, representing them as a population of flat circular pancakes, all with the same radius, expanding linearly with varying fractions of the Hubble flow and having random inclinations on the sky (Fig. 14). This model may seem unrealistic (and in fact, it is less sophisticated than the similar attempt by Charlton et al.), but there are several reasons to believe that it is a viable first step toward measuring the effect we are after, the Hubble expansion of the IGM. First, any sample of absorption lines is dominated by the objects with the largest geometric cross section, so a pancake is the best choice for a given radius. Second, homologous (i.e., velocity $\propto$ length) Hubble expansion may be a good assumption for sheets in the general IGM because the overdensities are moderate and structures are not expected to have collapsed in their longest linear dimension. The assumption of only one radius for the pancakes (as opposed to a distribution of radii) is more questionable, as a finite radius for a tilted expanding pancake corresponds to an upper limit in the velocity shear and introduces a cutoff in the distribution of velocity differences, so we need to apply some caution and not consider velocity shear beyond a certain value.

The projected velocity shear Δv between two lines of sight separated by a proper beam separation b, hitting a circular pancake-shaped cloud that expands radially with expansion velocity $v_{\rm exp} = rH(z)b(z)$ at an inclination angle α ($\alpha = 0$ would be face-on) and with an azimuthal angle ϕ (Fig. 15), is given by

$$\Delta v = rH(z)b(z)\tan\alpha\,\sin\phi. \tag{10}$$

Here $H(z)$ is the Hubble constant at redshift z, and the Hubble ratio r is defined as the ratio of the expansion velocity of the pancakes to the Hubble expansion (i.e., $r = v_{\rm exp}/v_{\rm Hubble}$; $r = 1$ would be pure Hubble flow).

Introducing the angular separation between the beams, $\Delta\theta$, and the angular diameter distance, D_A, this can be written

$$\frac{\Delta v}{\Delta\theta} = rH(z)D_A(z)\tan\alpha\,\sin\phi. \tag{11}$$

Adopting the nomenclature used by McDonald & Miralda-Escudé (1999) in their work on the Alcock-Paczyński test,[12] we split off the cosmological dependence of Δv and write it as

$$f(z) = \frac{H(z)D_A(z)}{c}. \tag{12}$$

[12] There have been a number of suggestions to exploit the Alcock-Paczyński effect using paired Lyα forest sight lines to derive cosmological parameters (e.g., McDonald & Miralda-Escudé 1999; Hui et al. 1999; Rollinde et al. 2003, Lidz et al. 2003). Essentially, this measurement employs autocorrelation and cross-correlation functions of the absorbed flux in the Lyα forest to measure a function of cosmological parameters (especially Λ) only.

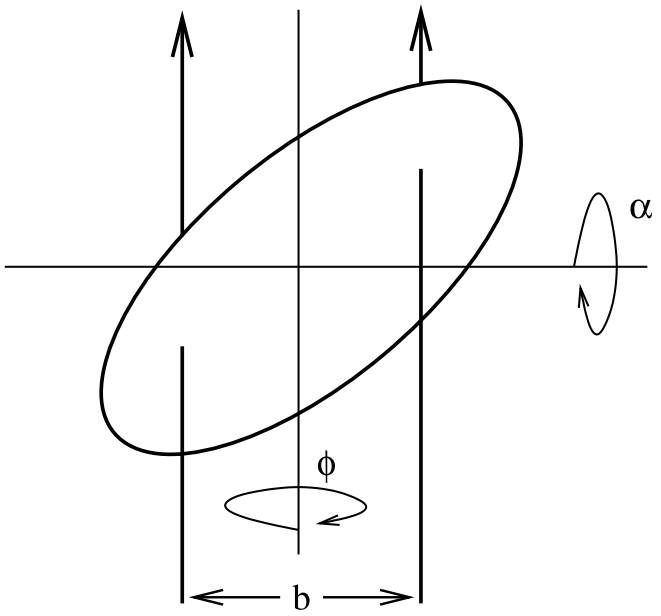

FIG. 15.—Homologously expanding pancake intersected by two lines of sight. The normal vector on the pancake surface is tilted with respect to the direction of the lines of sight by an angle α, and the tilt axis is rotated relative to the connecting line b between the lines of sight by an angle ϕ.

Our relation for the angular velocity shear becomes

$$\frac{\Delta v}{\Delta \theta} = rcf(z) \tan \alpha \sin \phi. \quad (13)$$

The idea is now to fit the observed distribution of Δv for absorption lines, trying to reproduce it with a model population of these pancakes hit at random orientations by imaginary double lines of sight. The ratio $r = v_{\rm exp}/v_{\rm Hubble}$ is treated as the free fitting parameter. Note that the factor $f(z)$ and thus the width of the distribution of Δv is independent of the absolute value of the Hubble constant. This is because the beam separation b is only known to within a factor h^{-1} (the angular diameter distance that enters in the calculation of b is proportional to c/H), and the velocity shear is proportional to bH. Thus the result of this measurement is the ratio r, which tells us about any departures from the Hubble flow but does not give the value of H. We will assume that $f(z)$ is completely known, i.e., that we know already the cosmological parameters reasonably well, and we ascribe any departures of r from unity to local departures from the Hubble flow. In fact, such departures are expected because typical, unsaturated Lyα clouds are moderately overdense and are thought to have collapsed in one dimension and thus should expand anisotropically, on a sufficiently small scale. In general, a column density–limited sample of absorption lines observed across a finite spatial scale smaller that the typical coherence length will never be representative of the free Hubble flow.

A Monte Carlo simulation of pancake-shaped "clouds" was used to create a distribution $P(\Delta v)$ of the velocity shear, given simultaneous hits of the same pancake by both lines of sight. The pancakes' normal vectors were randomly oriented with respect to the sight lines, and the hits were weighted with the projected geometric cross section subtended by the pancakes. The velocity differences projected along the line of sight between the points of the pancake hit by the lines of sight where gathered to form a theoretical frequency distribution of the velocity shear.

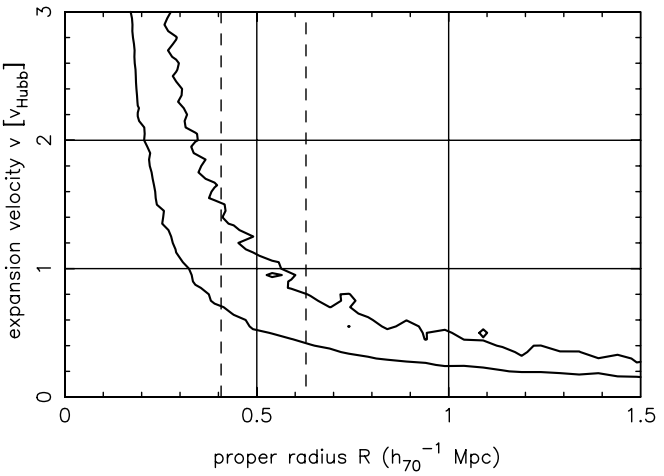

FIG. 16.—Solid lines are the χ^2 contours ($\pm 3\ \sigma$) for the maximum likelihood fit of the expanding pancake model to the velocity shear distribution at $z \approx 2$ (see Fig. 11), with the expansion velocity in units of the Hubble velocity and the proper radius of the pancakes as free parameters. The vertical dashed lines give the $\pm 3\ \sigma$ limits for the radii of the absorbing structures from D'Odorico et al. (1998). According to this plot, the average expansion of the Lyα forest at mean redshift $\langle z \rangle = 2.04548$ is $v = (0.8 \pm 0.3) v_{\rm Hubble}$ ($\sim 3\ \sigma$).

In practice, equation (10) shows that because of the nature of the Hubble law there is a degeneracy between line of sight extent and expansion velocity; a larger velocity of expansion and a smaller tilt of the pancake with respect to the observer give the same velocity shear as a smaller velocity of expansion and a larger tilt. Larger pancakes admit larger tilts leading to a larger Δv. The degeneracy is not perfect because of the finite size of the absorbers, but it is clear that if we wish to extract the velocity of expansion from the observations we need to have prior knowledge of the size of the absorbers. Numerous such measurements have been done (see § 1). We are using here the compilation by D'Odorico et al. (1998), who found the mean proper radius of Lyα clouds to be $R = 412\ h_{100}^{-1}$ kpc. In agreement with earlier work (Crotts & Fang 1998) these authors found no evidence of redshift evolution in the mean size. Transforming the D'Odorico et al. (1998) values to the cosmological model used here gives a mean radius $R = 503.5\ h_{70}^{-1}$ kpc, with $3\ \sigma$ limits ($407\ h_{70}^{-1}$ kpc $< R < 628\ h_{70}^{-1}$ kpc).

We model the Lyα forest as homologously expanding pancakes with a *constant* physical radius at all redshifts ($z \sim 2.04$–3.8) in our sample. The adoption of a constant physical size for an expanding object may sound counterintuitive, but we are really comparing common absorption systems *above a certain column density threshold* that is given by observational constraints and does not depend on redshift. Aside from the observational evidence cited above, theoretical arguments suggest that the linear, physical extent R of a Lyα absorber for a given column density depends only weakly on redshift. The dependence arises mainly through the ionization rate Γ according to $R \propto \Gamma^{-1/3}$ (e.g., Schaye 2001), which does not appear to change by more than 50% from redshift 4 to 2 (Rauch et al. 1997b), so that the change in radius at constant column density is less than 15%. Thus, using a single radius for the model pancakes is not entirely unjustifiable.

The results of maximum-likelihood–fitting the expanding pancake model to the observed velocity shear distributions are shown in Figures 16 and 17. The former gives the $3\ \sigma$ χ^2 contours for the best-fitting combination of proper radius and expansion velocity in units of the Hubble velocity for the Q2345+005AB lines of sight. Adopting the D'Odorico et al. (1998)

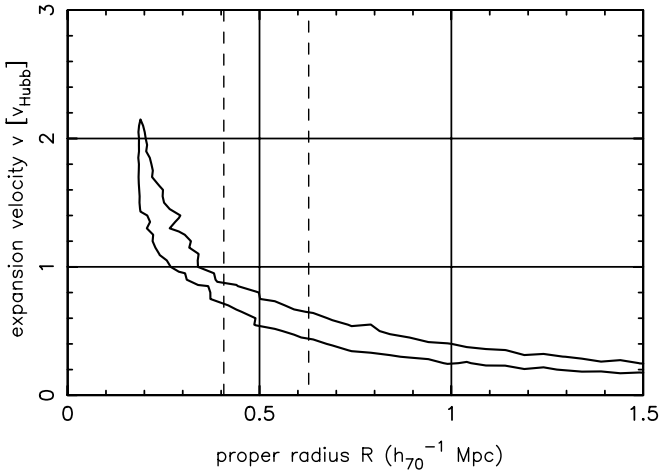

FIG. 17.—Solid lines are the χ^2 contours ($\pm 10\ \sigma$) for the fit of the expanding pancake model to the velocity shear distribution at mean redshift $\langle z \rangle = 3.53$ (see Fig. 12). Unlike the $z = 2$ case, in the present case these error contours are meaningless, as the total error is dominated by the uncertainty in the cross identification of absorption lines between the lines of sight. The vertical dashed lines again give the $\pm 3\ \sigma$ limits for the radii of the absorbing structures from D'Odorico et al. (1998). According to this plot, the average expansion of the Lyα forest at mean redshift $\langle z \rangle = 3.53$ is $v = (0.65 \pm 0.4) v_{\rm Hubble}$.

value for the radius, the best fit for the Hubble ratio is $r = 0.8 \pm 0.3$ ($3\ \sigma$). The corresponding theoretical curve with that value of r is shown overplotted as a solid line in Figure 11. For comparison, the curves for $r = 0.4$ (*dashed line*) and $r = 1.5$ (*dotted line*) are also shown. The $r = 0.4$ value produces a distribution too centrally condensed, whereas the higher value $r = 1.5$ gives too strong wings for the distribution. The main uncertainty in this (redshift $\sim$2) case comes from the finite number of absorption systems available in the spectrum. The fit for the higher redshift samples is given in Figure 12, with a formal best-fit value of $r = 0.65$. Here the statistical errors are small (we are showing the 10 σ contours!) but the main (and systematic) uncertainty comes from the confusion between unrelated systems and from missing the largest velocity separations. These effects are not taken into account in producing the χ^2 contours. From looking at individual absorption-line systems and redoing the line selection repeatedly on different subsets of the data, we estimate that the value could well be between 0.4 and 1.2, and we show these curves overplotted on the observed histogram in Figure 12, but even this error estimate itself is uncertain.

A better assessment of the reliability of these estimates of the Hubble ratio requires a more realistic model for the IGM, which we provide in the following section. We note, however, that a very simple model such as the expanding pancake reproduces the basic shape of the observed distribution of velocity shear quite well, and in combination with the best estimate of the coherence length for the Lyα forest clouds, it gives values of the expansion velocities for the moderately overdense IGM relatively close to the Hubble expansion.

5. A COMPARISON WITH COSMOLOGICAL HYDRODYNAMIC SIMULATIONS

To be able to gauge the meaning of our measurements of velocity shear (Figs. 11 and 12), and to understand how the velocities arise, we produced artificial Lyα forest spectra from a numerical cosmological hydrodynamic simulation. In such a simulation, the density and velocity field are of course known per definition, and it becomes possible to invert (in a primitive sense, at least) the spectrum to see which combinations of density, peculiar velocity, and Hubble expansion conspire to form a given absorption line, and, in close lines of sight, a pair of those. In particular, one can ask the questions, How do to the physical structures (gaseous filaments, etc.) expand or contract in order to give a certain distribution of velocity shear? And how do the considerable selection effects in the spectral domain affect the measurement of their velocities?

We use a new version of the parallel tree SPH (smoothed particle hydrodynamics) code GADGET (Springel et al. 2001) in its tree PM (particle mesh) mode, which speeds up the calculation of long-range gravitational forces considerably. The simulation is performed with periodic boundary conditions with 400^3 dark matter and 400^3 gas particles. Radiative cooling and heating processes are followed using an implementation similar to Katz et al. (1996) for a primordial mix of hydrogen and helium. The UV background is given by Haardt & Madau (1996). In order to maximize the speed of the simulation, a simplified criterion of star formation has been applied: all the gas at overdensities larger than 1000 times the mean overdensity is turned into stars (Viel et al. 2004). The simulation was run on COSMOS, a 152 GB shared memory Altix 3700 with 152 CPUs hosted at the Department of Applied Mathematics and Theoretical Physics (Cambridge). The cosmological parameters are $\Omega_m = 0.26$, $\Omega_\Lambda = 0.74$, $\Omega_b = 0.0463$, and $H_0 = 72$ km s^{-1} Mpc^{-1}. The ΛCDM transfer functions have been computed with CMBFAST (Seljak & Zaldarriaga 1996).

The comoving size of the box was 60 h^{-1} Mpc. At three different redshifts ($z = 2$, 3.4, and 3.8, close to the mean redshifts in the observations), 20 artificial lines of sight of lengths 5571, 6533, and 6789 km s^{-1} were run through the simulated box. The effective H I optical depth of the spectra was adjusted so as to match the phenomenological fitting formula given by Schaye et al. (2003) for each redshift. The lines of sight were created in pairs with transverse separations identical to the mean separations in our three observed QSO pairs, and there were 10 fake "QSO pairs" at each redshift. The Lyα forest spectra were subjected to the same analysis as the real data; i.e., spectral regions with assumed common absorption features in each pair were selected by eye and delineated with a cursor. A uniform minimum rest-frame equivalent width threshold of 0.4 Å was imposed, and the flux-weighted line-of-sight velocities were calculated.

Then all the spatial pixels along the line of sight whose total (= peculiar + Hubble) velocity projected into one of the selected absorption-line windows were identified. Their spatial positions (weighted by the square of the gas density, to emulate their contribution to the absorption-line optical depth) were used to obtain the spatial "centroid" along the line of sight of the gas clump causing the absorption in each pair spectrum. This procedure is crude in three ways: it ignores thermal motions and small-scale turbulence; it takes the recombination rate ("square of the density") as a proxy for optical depth; and it assumes that the Lyα forest lines typically are caused by overdensities, as opposed to velocity caustics (e.g., McGill 1990). The two former simplifications are clearly justified by us only attempting to measure the global shifts between entire absorption lines. The identification of most absorbers with overdensities (and rarely velocity caustics) is consistent with results from previous simulations (e.g., Miralda-Escudé et al. 1996).

Having obtained the spatial centroid where the density clump contributing most to a given absorption line intersects the two lines of sight, the relative three-dimensional velocity vector between these two positions is computed from the Hubble expansion and peculiar velocity array (Fig. 18). Thus, for each

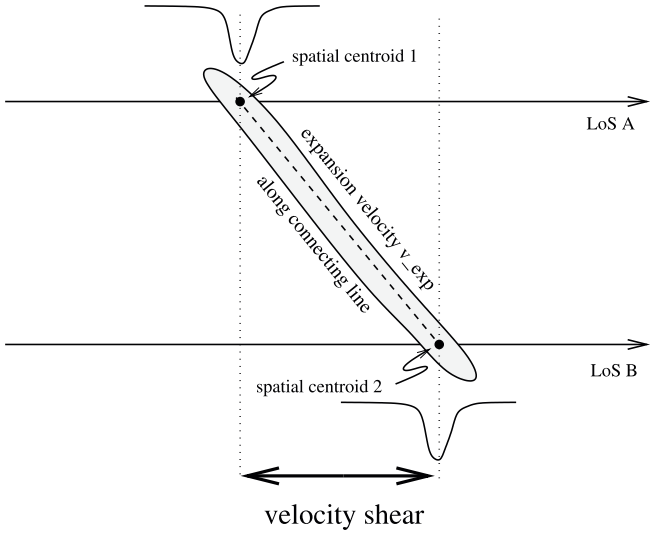

FIG. 18.—Illustration of the method for relating the velocity shear along the lines of sight to the expansion velocity of an absorption-selected gas cloud. (The figure is strictly valid only for pure Hubble flow, where the Hubble law guarantees that the angles and positions are the same in position space and velocity space.) Figs. 11, 12, 19, and 20 show the velocity shear, whereas Figs. 21, 22, and 23 show the distribution of the expansion velocity along the connecting line between the spatial centroids.

common absorption system in a pair of lines of sight, we know the three-dimensional relative velocity between the parts of the absorbing structure intersecting the lines of sight. It becomes possible to relate the observed, one-dimensional distribution of velocity shear to the three-dimensional motions of the IGM.

The resulting *simulated* shear distributions for $z = 2$ and 3.6 (the samples for $z = 3.4$ and 3.8 were combined to increase the statistics) are plotted as dotted histograms on top of the *real* data (same as in Figs. 11 and 12) in Figures 19 and 20. The only adjustment applied was for the integral of the curves to be the same. A Kolmogorov-Smirnov (K-S) test shows that the observed and simulated unbinned cumulative distributions of velocity shear are consistent with each other in the usual sense; i.e., the maximum differences between the cumulative distributions are expected to be exceeded in 30% ($z = 2$) and 15% ($z = 3.6$) of all random realizations, respectively. The rms velocity widths of the distributions are 16.6 km s^{-1} (observed) versus 14.9 km s^{-1} (simulated) in the redshift $z = 2$ case, and 30.0 km s^{-1} (observed) versus 30.6 km s^{-1} (simulated) in the redshift $z = 3.6$ case. The results are summarized in Table 1. The sample sizes are unfortunately not very impressive, but they are clearly enough to rule out underlying differences between the widths of the observed and simulated distributions at the 50% level. We conclude that the simulation reproduces both the observed *average* velocity shear and the observed *shape* of the one-dimensional distribution in the IGM quite well.

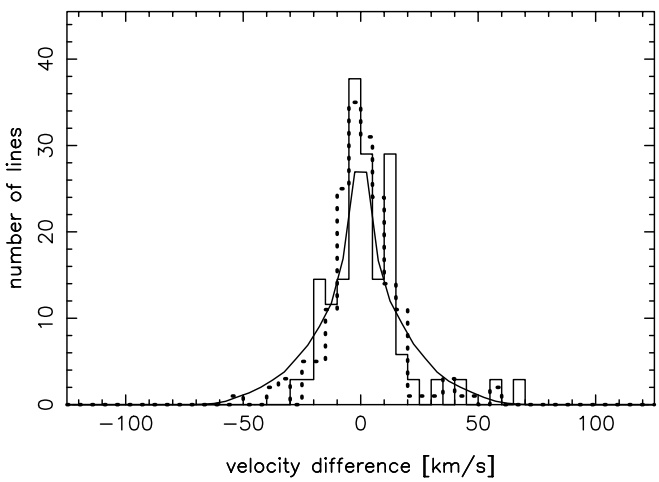

FIG. 19.—Observed distribution for Q2345+005 of Δv (*solid histogram*), the distribution from the hydrodynamic simulation for $z = 2$ (*dotted histogram*), and the best-fitting expanding pancake model, expanding with 0.8 times the Hubble velocity.

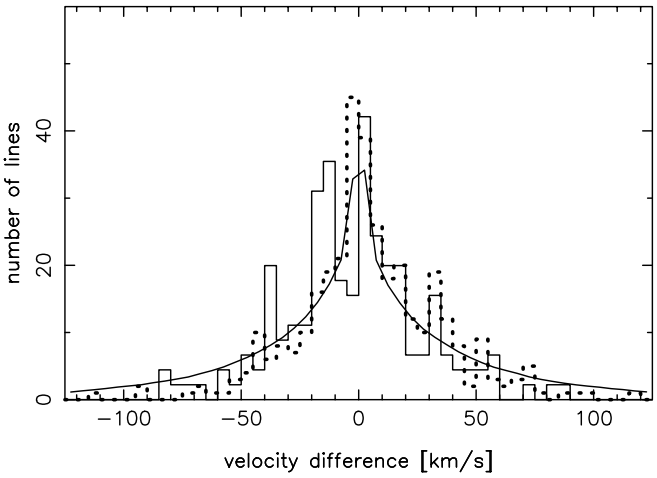

FIG. 20.—Same as Fig. 19, but with the solid histogram now showing the Δv measurements for the higher redshift ($\langle z \rangle \approx 3.6$) combined sample from the Q1439−0034AB pair and the Q1422+2309A/Q1422+2255 pair. Again the dotted line is from the simulation for mean redshift $\langle z \rangle = 3.6$, and the solid curve is the expanding pancake model for the same redshift with a Hubble ratio $r = 1.0$.

5.1. *The Theoretical Distribution of Expansion Velocities*

How does the underlying three-dimensional distribution of expansion velocities in the simulation look? Figures 21, 22, and 23 give the distributions of the simulated expansion velocities for redshifts 3.8, 3.4, and 2.0, respectively. To reiterate, these are the relative velocities of the two spatial centroids (along the line of sight) of gas clouds intersected by both lines of sight.

All three diagrams have some features in common. First, the most probable expansion velocity is larger than the Hubble expansion. The peak of the distribution falls into the $r_{\rm peak} = 1.15$ (1.15, 1.35) bins for the three redshifts. The median Hubble ratio is also larger than unity [$r_{\rm med} = 1.11$ (1.09, 1.08)]. There is a tail toward lower expansion velocities, even including a few physically contracting systems (with negative velocities). Interestingly, the tail grows more substantial with decreasing redshift, with the mean Hubble ratio going from $r_{\rm mean} = 1.03$ to 1.02 to 0.85 by redshift 2. This explains why the width of the $z = 2$ observed distribution of *velocity shear* seemed narrower than expected for pure Hubble expansion and why our 3 σ estimate of $r = 0.80 \pm 0.3$ from the expanding pancake model was smaller than unity (realistically, as it turns out).

For the higher redshift ($z \sim 3.6$), larger separation sample, the pancake model seems to have problems, though. As noted above, the mean Hubble ratio in the simulations (which give a velocity shear distribution very similar to the one from the real data) is above unity, but the fit with the pancake model at that redshift gave only an underestimate of $r = 0.65$. Most likely, the assumption of a nonevolving size for the pancakes, the finite sizes (relative to the transverse separations between the lines

TABLE 1
OBSERVATIONAL DATA VERSUS SIMULATIONS

ABSORPTION-LINE SAMPLE	$\bar{z}$	$H(z)$	$\bar{d}$ (h_{70}^{-1} kpc)	$(\Delta\bar{v})_{\rm rms}$ Observed	$(\Delta\bar{v})_{\rm rms}$ Simulated
RX J0911.4+055AB	2.57	243.7	0.82	<6.3	...
Q2345+007AB	2.04	195.2	61.0	16.6	14.9[a]
Q1422/1424 and Q1439AB	3.62	352.8	260.5	30.0	30.6[b]

NOTE.—Note that there are slight differences between the mean redshifts and the cosmological parameters adopted for the analysis of the data ($\Omega = 0.25$, $\Lambda = 0.75$, $h = 0.70$) and the simulations ($\Omega = 0.26$, $\Lambda = 0.74$, $h = 0.72$).
[a] The simulated distribution was obtained for $z = 2.0$.
[b] The simulated distribution is the mean from two simulations done at $z = 3.4$ and $z = 3.8$.

of sight), and confusion when cross-identifying absorbers, and thus incomplete counts at the largest velocity differences, are to blame.

In any case, the good agreement between the observed and theoretical distributions (Figs. 19 and 20) indicates that the same astrophysical mechanisms at work in the simulation are also present in nature; we are seeing direct evidence for breakaway from the Hubble flow and for gravitational collapse in some systems, the number of which increases dramatically when going to lower redshift.

In contrast to that, most Lyα forest systems continue to undergo super-Hubble expansion at all redshifts considered here. Filamentary or pancake-shaped structures expanding with super-Hubble velocities are a natural prediction of CDM-dominated structure formation scenarios (e.g., Haehnelt 1996) and have been proposed to be responsible for some of the largest velocity structures seen occasionally among metal absorption systems (Rauch et al. 1997b). These filaments occur at the boundaries of underdense "voids" that themselves expand faster than the Hubble flow. Another way of explaining super-Hubble expansion recognizes that filaments are being gravitationally stretched by and draining into the high-mass nodes terminating them (presumably future galaxy clusters), thus introducing super-Hubble velocity gradients.

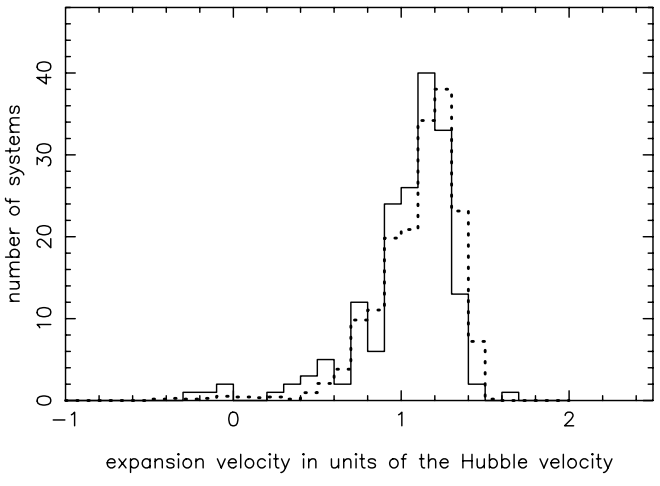

FIG. 21.—Expansion velocity in units of the Hubble velocity, along the straight line connecting the spatial absorption centroids (see Fig. 18) in the $z = 3.8$ simulation (*solid histogram*). Note the super-Hubble peak and the sub-Hubble tail indicating breakaway from the general expansion. Most clouds expand somewhat faster than the Hubble flow, but some have broken away and are even contracting. The dotted histogram applies to the expansion velocity measured at random positions along the line of sight (i.e., irrespective of there being an absorption line). There are only small differences between absorption-selected and random distributions (see text).

We caution that the numerical results and the distributions given here are obtained in a highly selective way: admitting only Lyα clouds with rest-frame equivalent widths above 0.4 Å selects denser gas at lower redshift that may be in a more advanced stage of collapse. In addition, the measurements differ simultaneously in redshift *and* beam separation (with mean physical separations of 236, 288, and 61 h_{72}^{-1} kpc for $z = 3.8$, 3.4, and 2.0). The expansion velocities are measured along straight lines between the density centroids selected by the absorption systems that they cause, so they do not take into account any curvature of the clouds, especially at the larger separations. Therefore the three histograms may be representing different density regimes, size scales, and cloud shapes at the three redshifts. They *do not necessarily correspond to an evolutionary sequence*.

We defer an assessment of the various selection effects and a discussion of the physical properties of the absorbers in the simulation to a future paper, but we can briefly ask the following question: in what sense do the motions of the objects in the simulation selected by their Lyα forest absorption differ from those of random regions in the universe? To construct a control sample of "random regions," we calculated the Hubble ratios between random (i.e., not absorption-selected) points along one line of sight and corresponding points in the "partner" line of sight at directions from the former that were drawn randomly from the distribution of orientations between the absorption-selected points. The results are overplotted as dotted histograms in Figures 21, 22, and 23 and summarized in Table 2.

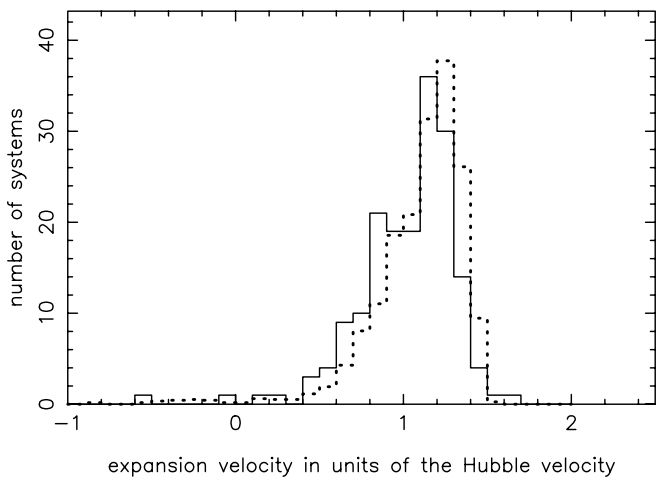

FIG. 22.—Same as Fig. 21, but for redshift 3.4. There is little change since redshift 3.8. However, gravitational collapse here has more noticeably decelerated the absorption-selected regions relative to the random ones. Note that there is a difference in redshift *and* beam separation between this plot and the previous and following ones.

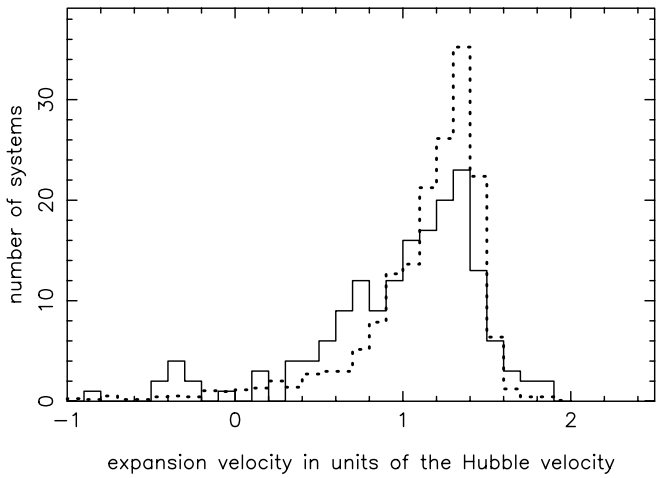

FIG. 23.—By redshift 2 and at the smaller (61 kpc) separation, gravitational collapse has broadened the distribution of Hubble ratios in absorption-selected regions (*solid histogram*), and there are now many regions expanding faster or slower than the Hubble flow. Random regions (*dotted histogram*) are more dominated by super-Hubble velocities characteristic of voids.

There is little difference at redshift 3.8, but already by $z = 3.4$ and much more so by $z = 2$ the distributions of the Hubble ratios have shifted considerably between random and absorption-selected regions. The mean Hubble ratios at redshifts 3.8, 3.4, and 2 are 1.03, 1.02, and 0.85 (absorption-selected) and 1.09, 1.09, and 1.08 (random), whereas the median Hubble ratios were 1.11, 1.09, and 1.08 (absorption-selected) and 1.15, 1.16, and 1.22 (random). Obviously, the overdense regions selected by the Lyα absorption are undergoing gravitational collapse faster than the random places. This is not surprising, as a random position in the universe is most likely to end up in underdense regions that expand faster than the Hubble flow. Note that the median Hubble ratio for the random regions is even increasing with decreasing redshift, presumably because it becomes harder to hit overdense regions with an ever-decreasing cross section.

6. LIMITS ON OTHER SOURCES OF MOTION IN THE INTERGALACTIC MEDIUM

Aside from pure Hubble expansion and motion in a gravitational potential well, one may expect galactic feedback, including galactic outflows, thermal expansion, or radiation pressure, or other hydrodynamic effects like ram pressure, to contribute to the motions in the IGM. There is now clear evidence that some of the above feedback processes must have led to widespread and early metal enrichment in the IGM. By redshift 3, much of the Lyα forest is metal-enriched (e.g., Cowie et al. 1995, Tytler et al. 1995, Ellison et al. 2000; Schaye et al. 2000, 2003; Songaila 2001; Simcoe et al. 2004). There is also evidence, at least for the stronger metal absorption systems, of recent injection of turbulent energy in the IGM, at the level of both the individual absorption lines and the entire absorption complexes (Rauch et al. 1996, 2001a). These findings point to the importance of the interactions between galactic potential wells and their IGM environment.

TABLE 2
HUBBLE RATIOS IN THE SIMULATIONS

		Absorption-selected Regions		Random Regions	
$\bar{z}$	d (h_{72}^{-1}kpc)	Mean r	Median r	Mean r	Median r
2.0.....	61	0.85	1.08	1.08	1.22
3.4.....	288	1.02	1.09	1.09	1.16
3.8.....	236	1.03	1.11	1.09	1.15

Of the above effects, galactic superwinds have perhaps received the most attention. These winds have primarily been seen close to the star-forming regions they originate in (McCarthy et al. 1987; Franx et al. 1997; Pettini et al. 2001, 2002; Heckman 2002), but based on their large power and analogies with low-redshift superwinds, it has been proposed that they may be able to escape galaxies and profoundly affect the properties of the IGM, blowing bubbles of highly ionized, metal-rich gas out to distances of more than half a Mpc (comoving; Adelberger et al. 2003; Cen et al. 2004). The first instances of individual superwinds actually *leaving* high-redshift galaxies may have been seen in Mg II (Bond et al. 2001a, 2001b) and O VI (Simcoe et al. 2002) absorption systems. It is less clear whether such winds would be common and/or strong enough to significantly alter the properties of the IGM. Simulations suggest that their impact may mostly affect very high column density systems (with neutral hydrogen column densities $N_{\rm H\,I} > 10^{16}$ cm^{-2}; Theuns et al. 2001). Searches for proposed signatures of cosmological wind shells (Chernomordik 1988) in the autocorrelation function of the Lyα forest have not been successful (Rauch et al. 1992). Employing differential measurements across close lines of sight, Rauch et al. (2001b) concluded that the general IGM (unlike rare, strong metal absorption systems) does not show the small-scale density structure likely to be associated with the recent passage of winds across the lines of sight.

It is tempting to revisit this question here and see whether the *velocities* in the IGM can shed new light on the impact (or otherwise) of such superwinds. We first briefly consider the likely observational signature of such outflows in the general IGM, and then ask specifically the question as to whether the observed velocity distribution of Lyα forest clouds can be affected by winds.

6.1. *The Observability of Cosmic Superwinds*

While the actual wind material from superwinds is too hot to be seen in absorption by UV resonance lines, there are a number of ways in which winds may be associated with lower ionization gas detectable as QSO absorption lines: winds may produce shells of swept-up IGM gas; they may entrain and expel ISM; they may disturb the density field of the ambient IGM and impart kinetic energy to it.

The detection of winds in the Lyα forest employed here relies on measuring these effects as differences between the appearance of the same absorber between multiple, relatively close sight lines.

Rauch et al. (2001b) used "cosmic seismometry" (i.e., expected transient differences in optical depth or column density between adjacent lines of sight) to limit the filling factor of winds in a simple toy model. Column density variations across the lines of sight may conceivably arise either directly from the passage of wind material, when small-scale entrained matter or a swept-up shell of IGM are intersected, or they may appear when the undisturbed external IGM gets hit by the shock front. For the range of mechanical energy and the ambient density associated with typical galactic superwinds, the swept-up shell should in principle contain enough H I to be seen in absorption (if it is photoionized), but the detectability depends crucially on the ionization mechanism. The cooling times for very energetic winds may be too long to produce a lot of neutral hydrogen

(e.g., Bertone et al. 2005), and one may have to resort to observing higher ions (e.g., O VI; Simcoe et al. 2002). The entrained matter should, however, be more easily visible in absorption because of the high density of the ISM where it came from, and because it is likely to dominate the mass of the ejecta (e.g., Suchkov et al. 1996). It is not clear whether results from low-redshift winds provide any reliable guidance to $z \sim 3$ winds, but such observations show that the entrained material is even visible in the Na I $\lambda\lambda$5890, 5896 doublet (e.g., Phillips 1993; Rupke et al. 2002; Martin 2005). Depending for its formation on largely neutral gas, Na I is one of the rarest ions seen in QSO absorption spectra. If it is present, many other ions are likely to be much more conspicuous.

6.2. *The Kinematic Signature of Superwinds*

Even if most superwinds were simply materially invisible in absorption and would not produce cold shells, or would evaporate all the entrained matter, the expanding bubble should have a kinematic impact on the surrounding IGM and accelerate the ambient H I containing gas. The acceleration should lead to detectable shifts of the absorption lines caused by clouds in the path of the wind, independently of whether they were produced by the wind (as cooling shells or entrained gas) or were present already before, e.g., in the form of gravitationally collapsed filaments. To estimate the order of magnitude of the wind velocities consistent with the observations, we adopt a simple model where a spherical shell of gas is pushed radially outward by a wind. It is pierced by two randomly oriented lines of sight and shows up observationally in the form of two absorption lines shifted relative to each other in each of the two lines of sight (Fig. 24). We focus our attention on the comparison of velocity differences arising on the same side of the shell, as a wind bubble wall is more likely to be spatially coherent over small distances than at opposing sides of a bubble. However, in the case of a spherical bubble the optimal transverse beam separation that maximizes the observable velocity shear is of course on the order of the radius of curvature of the wind front, which for galactic superwinds may be tens of kiloparsecs. Beam separations much smaller than that would show only small velocity differences.

Thus, with a separation on the order of 60 physical kpc between the lines of sight, Q2345+007AB is the most suitable QSO pair in our sample because it is comparable to the radii of shells proposed to exist around Lyman break galaxies and should deliver the strongest constraints on the presence of velocity shear.

The observed distribution of velocity differences between the absorption systems in the lines of sight to Q2345+007AB was given in Figure 11. The observed rms velocity differences for Q2345+007AB are $\Delta v = 16.6$ km s^{-1}, and this number can serve as the upper limit on the admissible velocity shear from winds. As discussed above, we assume that these velocity shifts are caused by Lyα forest absorbers pushed around by winds. We model the absorbers as spherically expanding, gaseous shells with radius R and expansion velocity $v_{\rm exp}$. The expected velocity shear Δv between the projected velocities of absorption lines measured between two lines of sight intersecting a shell can be written as a function of R, $v_{\rm exp}$, and various geometric quantities,

$$\Delta v = v_{\rm exp}\left(\sqrt{1-\frac{b_1^2}{R^2}} - \sqrt{1-\frac{b_1^2 + d^2 - 2b_1 d\cos\phi}{R^2}}\right). \quad (14)$$

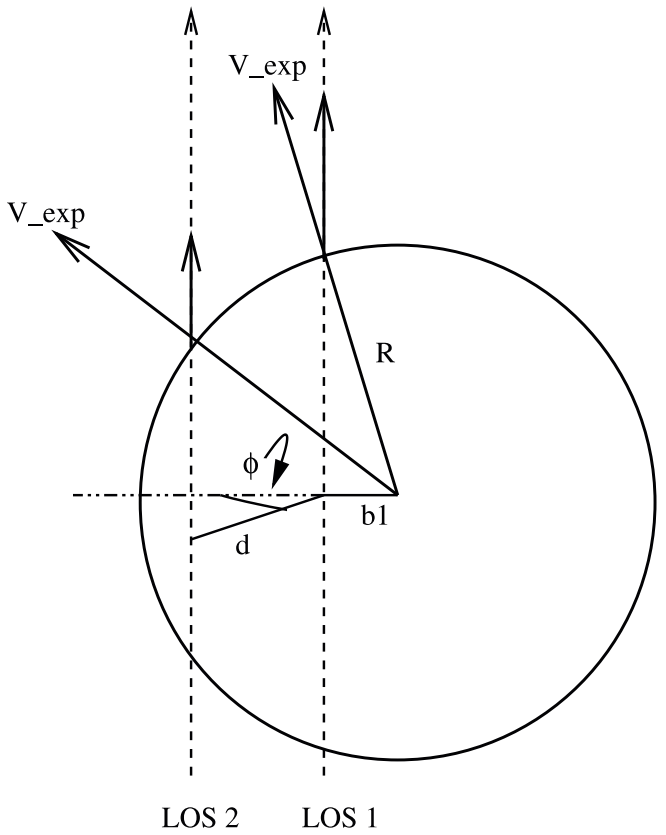

FIG. 24.—Velocity shear arising from projection effects when an expanding bubble is intersected by two lines of sight to background QSOs.

Here b_1 is the impact parameter of one of the lines of sight with respect to the center of the shell, d is the transverse separation between the lines of sight, and ϕ is the angle giving the relative orientation of the lines of sight with respect to the line connecting the first line of sight to the center of the shell.

First we ask which combination of radius and expansion velocity gives the same rms velocity difference as the observations. We have calculated the quantity Δv for a range of bubble radii from 30 to 230 kpc proper, based on a Monte Carlo simulation of impact parameters and relative orientations between the two lines of sight. The results are given in Figure 25. Any wind bubble with a radius-velocity combination on this graph will give a distribution of velocity differences with rms $= 16.6$ km s^{-1}, as observed. The admissible expansion velocities range between about 45 and 85 km s^{-1}, and have to be compared to the $v_{\rm exp} \sim$ 600 km s^{-1} and radii of up to 125 kpc (proper) proposed for winds strong enough to deplete the neutral hydrogen around Lyman break galaxies by evacuating the H I gas (Adelberger et al. 2003).

Going a step further, we can compare the *shape* of the actually observed distribution of velocity differences from Q2345+007AB to the hypothetical ones for expanding bubbles with different parameter combinations. Figure 26 shows the cumulative probability distributions for the observed and simulated velocity differences versus the velocity differences in units of the expansion velocity. The thin lines dropping smoothly to larger velocities are the models (comprising a single population with fixed radius and expansion velocity; the radii are given in the top right-hand corner of the plot), and the ragged histograms are the observed distribution of Δv. There is obviously only one observed distribution, which, however, can be modeled either as

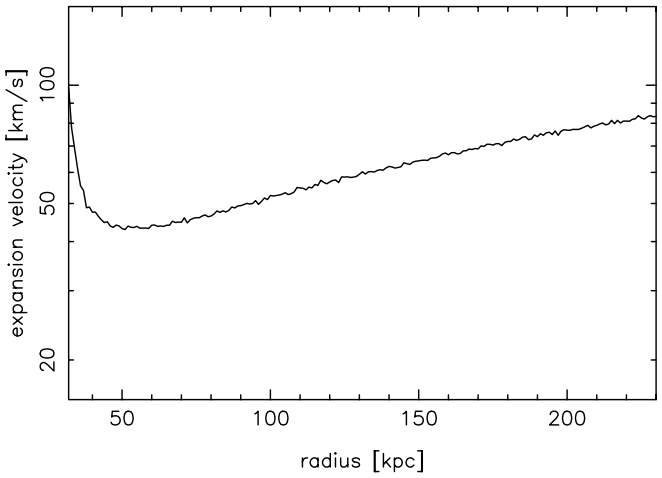

FIG. 25.—Relation between radius and expansion velocity for expanding $z = 2$ bubbles capable of producing the mean of the observed distribution of velocity differences, 16.6 km s^{-1}.

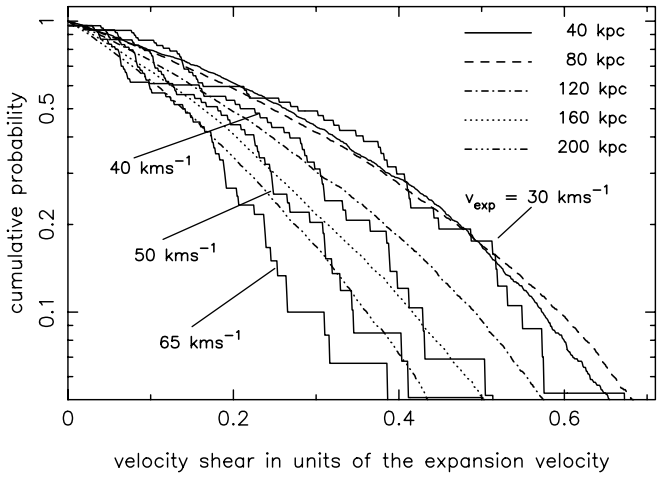

FIG. 26.—Cumulative distribution of velocity differences (in units of the radial expansion velocity v_{exp} for bubble models with proper radii 40, 80, 120, 160, and 200 kpc. The thick solid lines show the actually observed distribution (see also Fig. 11) scaled along the x-axis to match the model distributions for expansion velocities 30, 40, 50, and 65 km s^{-1}.

arising in a population of small bubbles (in which case the velocity differences would be a relatively large fraction of the expansion velocity) or as arising from larger bubbles (where the expansion velocity would have to be larger and the velocity differences would constitute a smaller fraction of the expansion velocity). The measurable velocity difference is linear in the expansion velocity, so we can scale the observed cumulative distribution until it matches best a particular combination of radius and expansion velocity. It can be seen that reasonable matches can be produced between either the bulk of the distributions or their respective wings, for radius-velocity combinations similar to the ones discussed in connection with the previous figure, but a single population of bubbles is not a good match. We cannot proceed any further here without explicitly assuming a distribution of windshell parameters, which is beyond the scope of this paper. The discrepancy could be either because a more realistic distribution of bubble radii and velocity is required or because the velocity structure of the Lyα forest has nothing to do with expanding bubbles.

If Lyα clouds were indeed bubble walls or at least owed their motions to winds, we can get a crude upper limit on the energetics of these winds. Assuming that the winds follow a simple expanding shell model like the one discussed by Mac Low & McCray (1988), the knowledge of the radius of the bubble R and the expansion velocity v_{exp} gives a constraint on the "strength" L_{38}/n_{-5} of the wind:

$$\left(\frac{v_{exp}^3}{157\ \mathrm{km\ s^{-1}}}\right)\left(\frac{R^2}{2670\ \mathrm{pc}}\right) = \frac{L_{38}}{n_{-5}}. \qquad (15)$$

Here L_{38} is the mechanical luminosity (in units of 10^{38} ergs) and n_{-5} is the particle number density of the surrounding IGM (in units of 10^{-5} cm^{-3}), assumed to be homogeneous.

A bubble with approximate radius 125 kpc and expansion velocity 55 km s^{-1} compatible with Figure 25 would thus have a strength of only $L_{38}/n_{-5} \sim 94$, i.e., a hundredth of what would be required if winds from Lyman break galaxies were getting out as far as postulated. Even assuming the largest radii shown in the diagram, 230 kpc, and velocities consistent with the observations, the strength of the wind falls short by an order of magnitude. The model applied here is of course hopelessly naive, but a more realistic assumption can only make the discrepancy worse. Assumptions of spherical geometry aside, the energy requirements to get a wind bubble out to a certain radius are certainly much more exacting when density gradients, infall, and the need to propel entrained matter are included. Moreover, our estimate for the maximum velocities admitted is of course conservatively high, as we assumed that all the velocity shear of 16.6 km s^{-1} arises in winds, and nothing in the Hubble flow or through gravitational motions.

6.3. *Where Are the Winds?*

If our assumption about the detectability of winds is correct, then we are led to conclude that winds by the time we observe them are either too weak or too rare to make an impact on the general IGM.

If high-redshift galactic winds are to be common enough to upset the gravitational instability picture of the Lyα forest and be consistent with our observations, the winds must be rather "limp" or "tired," quite different from the hundreds of km s^{-1} expansion velocities seen in Lyman break galaxy outflows or in the component structure of O VI absorbers. Recent theoretical work (Madau et al. 2001; Furlanetto & Loeb 2003; Fujita et al. 2004; Bertone et al. 2005) indicates that the inclusion of infall and entrained matter may slow down galactic winds considerably from the hundreds of km s^{-1} seen directly in the cores of starbursting galaxies to velocities on the order of a few tens of km s^{-1}, values consistent with our upper limits of 45–85 km s^{-1} (Fig. 25), so the observed velocity range in itself is not a problem. Are we then seeing wind-driven gas in the Lyα forest? The answer is, most probably not. As seen above, the Hubble expansion plus gravitational collapse does already explain all the observed velocity shear well, at three different redshifts and separations ranging from subkiloparsec to 300 kpc scales. If the observed velocity dispersion were dominated by winds, one would have to explain why the Hubble and gravitational motions are irrelevant and how the winds conspire to mimic exactly the velocity field in a ΛCDM universe without any feedback.

Nevertheless, a generation of old and possibly very widespread winds, perhaps connected to the reionization process and to an early phase of heavy-element production, need not be inconsistent with our observations, if the residual velocities are smaller than the limits given here and if pressure equilibrium is able to erase the

column density differences between the lines of sight. The observed very early metal enrichment (Songaila 2001; Pettini et al. 2003), its relative uniformity (Aguirre et al. 2005), the observed mass-metallicity relation (Tremonti et al. 2004), and the theoretical difficulties of getting metals out of massive galaxies (Scannapieco et al. 2002; Furlanetto & Loeb 2003; Fujita et al. 2004; Scannapieco 2005) all appear to favor an abundance of dwarf galaxies venting their metal-enriched gas early on. Pushing the hydrodynamic disturbances associated with the metal enrichment to an early epoch, the close resemblance of the properties of the Lyα forest to the predictions of a hierarchical scenario can be more easily reconciled with the relatively widespread metal enrichment observed. For example, if winds carried metal-enriched gas to the outer edge of filaments (say to radii of 40 kpc proper) and ceased shortly after the epoch of reionization (after $z \sim 6$), there would be enough time (1.2 Gyr) until the redshift of observation ($z \sim 3$) for the gas to have slipped back into the unaltered CDM potential wells, even at subsonic speeds.

Alternatively, strong winds active at the epoch that we observe (including but not limited to superwinds from Lyman break galaxies) may also be consistent with our observation if the filling factor of winds is small enough to not impact the IGM significantly. In the absence of realistic wind models it is difficult to use observations to constrain the filling factor of winds (for an attempt, see Rauch et al. 2001b), but there are some independent pieces of evidence. If, as Simcoe et al. (2002) have suggested, the strong O VI absorbers in their survey are experimentally identified with galactic wind bubbles from Lyman break galaxies, we have approximately 12 O VI systems at 40% completeness over a redshift distance $dX = 6.9$, or 4.3 systems per unit redshift. Over the same redshift distance there are about 132 low column density ($10^{12.5}$ cm$^{-2} < N < 10^{14}$ cm^{-2}) ordinary Lyα absorption systems at $z \sim 2.1$ (Kim et al. 2002). Thus, the relative rate of incidence of wind bubbles to intersections with the general cosmic web would be about 3%. This would be the fraction of the *volume producing the Lyα forest* that is occupied by winds. It is still possible that winds fill a larger *cosmic volume* if they are collimated (e.g., De Young & Heckman 1994; Theuns et al. 2002) and are preferentially blowing perpendicular to the filaments into the voids. The density gradients into the voids would ease the directional expansion of the hot gas but would also make detection of this gas with any method very hard. On the other hand, if such winds were limited to the same structures causing the Lyα forest, they could also occupy an even smaller *cosmic volume* than the 3% of the cosmic web, in particular if they are strongly clustered. Theuns et al. (2002), Pieri & Haehnelt (2004), and Desjacques et al. (2004), attempting to reproduce the C IV metal distribution, the observed incidence of weak O VI, and the sizes of the Adelberger et al. (2003) bubbles, respectively, have argued that the cosmic volume filling factor of Lyman break winds is likely to be only on the order of few percent. Figuratively speaking, they are just storms in intergalactic teacups. Disturbances that rare would not have affected the velocity distributions discussed above above, no matter how important their local impact.

6.4. *Alternative Explanations: Winds or Gravitational Motions?*

The results discussed here constrain the impact of winds on the IGM, but they do not rule out their existence. The original arguments for the existence of high-redshift winds (large velocity shifts between emission and absorption lines, possible production sites for the bulk of metals) are certainly persuasive, but the evidence often quoted as proving the impact of winds on the IGM appears more ambiguous. It is worth speculating whether some of the evidence proposed in favor of superwinds escaping from $z \sim 3$ galaxies does not admit alternative interpretations.

Adelberger et al. (2003) originally suggested that large zones with relatively little H I absorption near $z \sim 3$ Lyman break galaxies are the consequence of winds evacuating neutral hydrogen within radii on the order of 125 kpc (proper). While this result has proven hard to explain theoretically with any astrophysical effect, the new, larger data set presented by Adelberger et al. (2005) proposes smaller radii (40 kpc) for the average evacuated superwind bubble. We note here that this is essentially the same size derived by Simcoe et al. (2002) for strong O VI absorbers at similar redshifts, under the assumption that each absorber is a bubble of highly ionized gas around a Lyman break galaxy. While there seems to be agreement about the size of the effect, the origin of these regions remains less clear.

Gas heated by compression during gravitational collapse would appear similarly as a halo with a low fraction of neutral H I gas. In fact, unlike winds, gravitational heating *must* take place at some stage during the formation of every galaxy, especially in hierarchical structure formation where protogalaxies accrete gas while frequently merging with supersonic velocities, shocking the ambient gas. Judging from the analysis of SPH simulations of forming galaxies (e.g., Rauch et al. 1997a, Fig. 1), such hot halos or shocked shells with temperatures of several times 10^5 K are common even around individual merging galaxies at $z \sim 3$, with radii of 30–60 kpc proper. By $z \sim 2$ gaseous halos with temperatures up to 10^6 K start engulfing entire groups of these protogalactic clumps, and hotter, more spherical large halos with an extent on the order of 50–100 kpc form quickly around massive galaxies within times on the order of 10^9 yr. To explain the factor of 7 decrease in optical depth at the centers of the H I–poor bubbles observed by Adelberger et al. (2003) by increased thermal ionization would require a rise in temperature by only 1 order of magnitude (e.g., from 10^4 to 10^5 K for gas overdense by a factor of 10, and less for less dense gas; e.g., Haehnelt et al. 1996, Fig. 2), which is obviously well within what gravitational heating can do. In the simulation, the evolution to a more spherical, larger hot halo is rapid (essentially the constituents of a future galaxy are in free fall), with hot halos becoming a common feature below redshift 2, and becoming more common and larger as time proceeds. Keres et al. (2005) and Birnboim & Dekel (2003) discuss bimodal galaxy formation in which part of the galaxy population is fed by accreting gas with instant cooling, avoiding shock heating during infall, whereas another subpopulation grows by the more orthodox, shocked infall of gas. In any of these scenarios the fraction of galaxies with hot accretion must be increasing with time, which may provide an observationally testable prediction. Hot gas halos are also a basic ingredient in analytical models where cool gas is fed to a growing galaxy in a multiphase thermal instability (e.g., Mo & Miralda-Escudé 1996; Maller & Bullock 2004).

It appears that the partial destruction of galaxies in the hierarchical structure formation scenario would also lead to enhanced IGM metallicities, as observed in the immediate, high-density vicinity of galaxies (e.g., Simcoe et al. 2002, 2005). Gnedin (1998) has argued that mergers, through collision, tidal interactions, and ram pressure stripping, may be responsible for part of the IGM metal enrichment.

Other arguments for the impact of $z \sim 3$ Lyman break galaxies on the IGM have included the clustering of C IV systems around Lyman break galaxies, which, however, is only indicative of

spatial association of both the metals and the galaxies with the same matter overdensities and does not prove a causal connection, i.e., an outflow of the metals out of the same galaxies (e.g., Porciani & Madau 2005). Given the large spatial extent of the metals, the latter is quite unlikely (Scannapieco et al. 2005).

We conclude, emphasizing that none of the above rules out high-redshift winds; we only suggest that their prevalence may be overestimated if the gasdynamical consequences of the hierarchical merger process are mistaken for winds.

7. DISCUSSION AND SUMMARY

We have measured the shear between the velocities of absorption systems common to close lines of sight to background QSOs. Over physical distances on the order of a kiloparsec, the observed distribution of the differences between the velocities projected along the line of sight is largely consistent with being mostly due to measurement error. A small fraction (on the order of 10% of all systems) show significant (at the 2.5 σ level) velocity shear. Inspection of the individual images shows that the motions mostly appear to be bulk shifts of the entire absorption system in the two lines of sight. The mean shift for the 10 largest deviations is 11 km s^{-1}, and the rms contribution to the total width of the distribution of shear is about 6 km s^{-1}. We speculate that we may be seeing rotational or other differential motion of gas "circling the drain" in a gravitational potential.

Proceeding to larger scales, we measure the velocity shear distribution in the Lyα forest toward three QSO pairs near mean redshifts 2 and 3.6, for mean separations (60–300 h_{70}^{-1} physical kpc) large enough to see evidence of the Hubble expansion. The measurement cannot give the absolute value of the Hubble constant, but only the relative motions of the gas in units of the local Hubble flow. With increasing separation, the shape of the observed distribution of shear begins to depart from the Gaussian (error-dominated) shape seen at kiloparsec separations. It shows broad wings as expected if the large-scale systematic motions take over. Indeed, a simple analytical model where the absorbers are homologously expanding, randomly oriented pancakes (e.g., Haehnelt 1996) gives a reasonable representation of the data. Adopting the mean coherence length from the literature (D'Odorico et al. 1998) for the diameter of the pancakes, the model indicates that the radial expansion velocity is reasonably close to but somewhat less than the expected Hubble expansion over that scale. In the case of the lower redshift ($z \sim 2$) data set, the best fit indicates that the model pancake would have to expand with 0.8 ± 0.3 (3 σ) of the local Hubble flow. Confusion (problems with cross-identifying the absorbers between the lines of sight) is still negligible at this redshift and beam separation, so we can consider this value as a relatively unbiased measurement whose main source of error is the finite number of absorbers. For the higher redshift sample the best fit gives a smaller value ($0.65 \times$ the Hubble velocity), but the large confusion involved and doubts about the validity of our assuming a nonevolving size for the pancakes make us suspect that the result is a systematic underestimate of the actual expansion velocity. We test these suspicions with a more sophisticated model using artificial lines of sight to probe the cosmic web in a cosmological hydrodynamic simulation of a ΛCDM universe without feedback, with observational parameters as close as possible to the observed situation. The results from this modeling confirm that the measurement of the expansion velocity with the constant-size pancake model applied to an absorption-line sample selected manually at $z \sim 2$ was quite realistic. They further confirm that the same approach indeed underestimates the expansion velocities beyond redshift 3. A K-S test shows that the observed and simulated distributions of velocity shear are consistent with being drawn from the same population. The observed rms widths of the velocity shear distributions, 16.6 km s^{-1} ($z = 2$) and 30.0 km s^{-1} ($z = 3.6$) closely resemble the values obtained from the hydrodynamic simulation (14.9 and 30.6 km s^{-1}, respectively), and the shapes of the distributions are virtually indistinguishable. The detailed agreement between the observed and simulated distributions of velocity shear may be taken to imply that whatever physical processes produce the simulated distributions must be present in reality as well.

We compute the underlying distribution of expansion velocities for *absorption-line–selected* regions in the simulation (the line-of-sight projection of which produces the distribution of velocity shear). This distribution shows most Lyα clouds expanding faster than the Hubble flow, but the mean velocity (at least at redshift 2 and probably below) is somewhat less that the Hubble velocity. The larger fraction of contracting clouds (in comoving coordinates) in the $z = 2$ sample as compared to the higher redshift samples may be due in part to deceleration with time or to the different spatial scales, but it could also be partly a selection effect. By imposing an equivalent width detection threshold constant in time, we may be selecting higher density, more collapsed regions at lower redshift.

The same distribution is also computed for *random* regions in the simulation. We find significant differences, in that the latter expand increasingly faster with decreasing redshift than the absorption-line–selected regions. Apparently, most regions selected by typical Lyα forest absorption lines show the large-scale kinematics expected of mildly overdense, large sheetlike or filamentary structures, most of which are draining with super-Hubble velocities into larger mass agglomerations, while some of them are undergoing gravitational collapse.

We briefly considered the possibility, occasionally raised, that the Lyα forest could be seriously affected by galactic feedback, especially galactic superwinds active at the epoch of observation. Given the close agreement between the observed velocity distribution and the one predicted by the standard ΛCDM-based gravitational instability scenario, we find little room for a cosmological population of superwinds significantly disturbing the density and velocity structure of the general IGM. While this does not rule out the existence of such winds, various strands of evidence suggest that any winds simply may have a small filling factor as far as the overdense IGM giving rise to the Lyα forest is concerned. To escape detection, high-redshift superwinds may be intrinsically rare, or could be venting preferentially into cosmic voids, or may be more limited in their individual spatial range and expansion velocity because of the vicissitudes of infall, entrainment, or the larger ambient density at high redshift.

A more widespread population of *early* winds could still be consistent with our measurement and several other recent constraints on the distribution of metals, as could a later population of "limp" winds with sufficiently low expansion velocities at the time we observe them.

Finally, it appears that much of the observational evidence usually presented in favor of superwinds in the IGM may not be unique (and may not even favor superwinds, at least as far as the process of metal enrichment is concerned). Hot halos formed naturally during accretion and mergers in a hierarchical galaxy formation picture may have observational properties in common with the H I depleted, metal-enriched bubbles ascribed to superwinds from massive galaxies. In individual cases, the underlying cause may be hard to ascertain, but the hierarchical scenario should predict a definite dependence of the radii and

rate of incidence of hot accretion halos with time, which may be tested with observations.

M. R. is grateful to Nick Gnedin for a stimulating discussion that rekindled his interest in cross-correlating Lyα forests. He further thanks the National Science Foundation for supporting this work under grant AST 00-98492. M. V. and M. R. thank the Kavli Institute for Theoretical Physics in Santa Barbara for its hospitality in 2004 December during the workshop on "Galaxy–Intergalactic Medium Interactions," supported in part by the NSF under grant PHY 99-07949. M. V. thanks PPARC for financial support. M. R. and G. D. B. thank the I. S. Bowen memorial fund for superior sustenance. The work of G. D. B. and W. L. W. S. was supported by the NSF through grants AST 99-00733 and AST 02-06067. The hydrodynamic simulation was done at the UK National Cosmology Supercomputer Center funded by PPARC, HEFCE, and Silicon Graphics/Cray Research.

REFERENCES

Adelberger, K. L., Shapley, A. E., Steidel, C. C., Pettini, M., Erb, D. K., & Reddy, N. A. 2005, ApJ, 629, 636
Adelberger, K. L., Steidel, C. C., Shapley, A. E., & Pettini, M. 2003, ApJ, 584, 45
Aguirre, A., Schaye, J., Hernquist, L., Kay, S., Springel, V., & Theuns, T. 2005, ApJ, 620, L13
Aracil, B., Petitjean, P., Smette, A., Surdej, J., Mücket, J. P., & Cristiani, S. 2002, A&A, 391, 1
Bade, N., Siebert, J., Lopez, S., Voges, W., & Reimers, D. 1997, A&A, 317, L13
Barlow, T. A., & Sargent, W. L. W. 1997, AJ, 113, 136
Bechtold, J., Crotts, A. P. S., Duncan, R. C., & Fang, Y. 1994, ApJ, 437, 83
Becker, G. D., Sargent, W. L. W., & Rauch, M. 2004, ApJ, 613, 61
Bertone, S., Stoehr, F., & White, S. D. M. 2005, MNRAS, 359, 1201
Birnboim, Y., & Dekel, A. 2003, MNRAS, 345, 349
Bond, N. A., Churchill, C. W., Charlton, J. C., & Vogt, S. S. 2001a, ApJ, 562, 641
———. 2001b, ApJ, 557, 761
Burud, I., et al. 1998, ApJ, 501, L5
Cen, R., Miralda-Escudé, J., Ostriker, J. P., & Rauch, M. 1994, ApJ, 437, L9
Cen, R., Nagamine, K., & Ostriker, J. P. 2004, ApJ, submitted (astro-ph/0407143)
Cen, R., & Simcoe, R. A. 1997, ApJ, 483, 8
Charlton, J. C., Anninos, P., Zhang, Y., & Norman, M. L. 1997, ApJ, 485, 26
Charlton, J. C., Churchill, C. W., & Linder, S. M. 1995, ApJ, 452, L81
Chernomordik, V. V. 1988, Soviet Astron., 32, 6
Cowie, L. L., Songaila, A., Kim, T.-S., & Hu, E. M. 1995, AJ, 109, 1522
Crotts, A. P. S., & Fang, Y. 1998, ApJ, 502, 16
Desjacques, V., Nusser, A., Haehnelt, M. G., & Stoehr, F. 2004, MNRAS, 350, 879
De Young, D. S., & Heckman, T. M. 1994, ApJ, 431, 598
Dinshaw, N., Foltz, C. B., Impey, C. D., Weymann, R. J., & Morris, S. L. 1995, Nature, 373, 223
Dinshaw, N., Impey, C. D., Foltz, C. B., Weymann, R. J., & Chaffee, F. H. 1994, ApJ, 437, L87
D'Odorico, V., Cristiani, S., D'Odorico, S., Fontana, A., Giallongo, E., & Shaver, P. 1998, A&A, 339, 678
D'Odorico, V., Petitjean, P., & Cristiani, S. 2002, A&A, 390, 13
Ellison, S. L., Songaila, A., Schaye, J., & Pettini, M. 2000, AJ, 120, 1175
Fang, Y., Duncan, R. C., Crotts, A. P. S., & Bechtold, J. 1996, ApJ, 462, 77
Foltz, C. B., Weymann, R. J., Röser, H.-J., & Chaffee, F. H., Jr. 1984, ApJ, 281, 1
Franx, M., Illingworth, G. D., Kelson, D. D., von Dokkum, P. G., & Tran, K.-V. 1997, ApJ, 486, L75
Fujita, A., Mac Low, M.-M., Ferrara, A., & Meiksin, A. 2004, ApJ, 613, 159
Furlanetto, S. R., & Loeb, A. 2003, ApJ, 588, 18
Gnedin, N. Y. 1998, MNRAS, 294, 407
Haardt, F., & Madau, P. 1996, ApJ, 461, 20
Haehnelt, M. G. 1996, in Cold Gas at High Redshift, ed. M. N. Bremer & N. Malcolm (Dordrecht: Kluwer), 109
Haehnelt, M. G., Rauch, M., & Steinmetz, M. 1996, MNRAS, 283, 1055
Heckman, T. M. 2002, in ASP Conf. Ser. 254, Extragalactic Gas at Low Redshift, ed. J. M. Mulchaey & J. T. Stocke (San Francisco: ASP), 292
Hernquist, L., Katz, N., Weinberg, D. H., & Miralda-Escudé, J. 1996, ApJ, 457, L51
Hui, L., Stebbins, A., & Burles, S. 1999, ApJ, 511, L5
Katz, N., Weinberg, D. H., & Hernquist, L. 1996, ApJS, 105, 19
Keres, D., Katz, N., Weinberg, D. H., & Davé, R. 2005, MNRAS, in press (astro-ph/0407095)
Kim, T.-S., Carswell, R. F., Cristiani, S., D'Odorico, S., & Giallongo, E. 2002, MNRAS, 335, 555
Kneib, J.-P., Cohen, J. G., & Hjorth, J. 2000, ApJ, 544, L35
Lidz, A., Hui, L., Crotts, A. P. S., & Zaldarriaga, M. 2003, preprint (astro-ph/0309204)
Lopez, S., Hagen, H.-J., & Reimers, D. 2000, A&A, 357, 37
Mac Low, M.-M., & McCray, R. 1988, ApJ, 324, 776
Madau, P., Ferrara, A., & Rees, M. J. 2001, ApJ, 555, 92
Maller, A. H., & Bullock, J. S. 2004, MNRAS, 355, 694
Martin, C. L. 2005, ApJ, 621, 227
McCarthy, P. J., van Breugel, W., & Heckman, T. 1987, AJ, 93, 264
McDonald, P., & Miralda-Escudé, J. 1999, ApJ, 518, 24
McGill, C. 1990, MNRAS, 242, 428
Miralda-Escudé, J., Cen, R., Ostriker, J. P., & Rauch, M. 1996, ApJ, 471, 582
Mo, H.-J., & Miralda-Escudé, J. 1996, ApJ, 469, 589
Monier, E. M., Turnshek, D. A., & Hazard, C. 1999, ApJ, 522, 627
Patnaik, A. R., Browne, I. W. A., Walsh, D., Chaffee, F. H., & Foltz, C. B. 1992, MNRAS, 259, 1P
Petitjean, P., Mücket, J. P., & Kates, R. E. 1995, A&A, 295, L9
Petitjean, P., Surdej, J., Smette, A., Shaver, P., Mücket, J., & Remy, M. 1998, A&A, 334, L45
Pettini, M., Madau, P., Bolte, M., Prochaska, J. X., Ellison, S. L., & Fan, X. 2003, ApJ, 594, 695
Pettini, M., Rix, S. A., Steidel, C. C., Hunt, M. P., Shapley, A. E., & Adelberger, K. L. 2002, Ap&SS, 281, 461
Pettini, M., Shapley, A. E., Steidel, C. C., Cuby, J.-G., Dickinson, M., Moorwood, A. F. M., Adelberger, K. L., & Giavalisco, M. 2001, ApJ, 554, 981
Phillips, A. C. 1993, AJ, 105, 486
Pieri, M. M., & Haehnelt, M. G. 2004, MNRAS, 347, 985
Porciani, C., & Madau, P. 2005, ApJ, 625, L43
Rauch, M., Carswell, R. F., Chaffee, F. H., Foltz, C. B., Webb, J. K., Weymann, R. J., Bechtold, J., & Green, R. F. 1992, ApJ, 390, 387
Rauch, M., & Haehnelt, M. G. 1995, MNRAS, 275, L76
Rauch, M., Haehnelt, M. G., & Steinmetz, M. 1997a, ApJ, 481, 601
Rauch, M., Sargent, W. L. W., & Barlow, T. A. 1999, ApJ, 515, 500
———. 2001a, ApJ, 554, 823
Rauch, M., Sargent, W. L. W., Barlow, T. A., & Carswell, R. F. 2001b, ApJ, 562, 76
Rauch, M., Sargent, W. L. W., Barlow, T. A., Weinberg, D. H., Hernquist, L., Katz, N., Cen, R., & Ostriker, J. P. 1997b, ApJ, 489, 7
Rauch, M., Sargent, W. L. W., Womble, D. S., & Barlow, T. A. 1996, ApJ, 467, L5
Rollinde, E., Petitjean, P., Pichon, C., Colombi, S., Aracil, B., D'Odorico, V., & Haehnelt, M. G. 2003, MNRAS, 341, 1279
Rupke, D. S., Veilleux, S., & Sanders, D. B. 2002, ApJ, 570, 588
Sargent, W. L. W., Young, P. J., Boksenberg, A., & Tytler, D. 1980, ApJS, 42, 41
Scannapieco, E. 2005, ApJ, 624, L1
Scannapieco, E., Ferrara, A., & Madau, P. 2002, ApJ, 574, 590
Scannapieco, E., Pichon, C., Aracil, B., Petitjean, P., Thacker, R. J., Pogosyan, D., Bergeron, J., & Couchman, H. P. M. 2005, MNRAS, in press
Schaye, J. 2001, ApJ, 559, 507
Schaye, J., Aguirre, A., Kim, T.-S., Theuns, T., Rauch, M., & Sargent, W. L. W. 2003, ApJ, 596, 768
Schaye, J., Rauch, M., Sargent, W. L. W., & Kim, T.-S. 2000, ApJ, 541, L1
Schneider, D. P., et al. 2000, AJ, 120, 2183
Seljak, U., & Zaldarriaga, M. 1996, ApJ, 469, 437
Sheinis, A. I., Bolte, M., Epps, H. W., Kibrick, R. I., Miller, J. S., Radovan, M. V., Bigelow, B. C., & Sutin, B. M. 2002, PASP, 114, 851
Simcoe, R. A., Sargent, W. L. W., & Rauch, M. 2002, ApJ, 578, 737
———. 2004, ApJ, 606, 92
Simcoe, R. A., Sargent, W. L. W., Rauch, M., & Becker, G. D. 2005, ApJ, submitted
Smette, A., Robertson, J. G., Shaver, P. A., Reimers, D., Wisotzki, L., & Koehler, T. 1995, A&AS, 113, 199
Smette, A., Surdej, J., Shaver, P. A., Foltz, C. B., Chaffee, F. H., Weymann, R. J., Williams, R. E., & Magain, P. 1992, ApJ, 389, 39
Songaila, A. 2001, ApJ, 561, L153
Springel, V., Yoshida, N., & White, S. D. M. 2001, NewA, 6, 79

Suchkov, A. A., Berman, V. G., Heckman, T. M., & Balsara, D. S. 1996, ApJ, 463, 528
Theuns, T., Mo, H.-J., & Schaye, J. 2001, MNRAS, 321, 450
Theuns, T., Viel, M., Kay, S., Schaye, J., Carswell, R. F., & Tzanavaris, P. 2002, ApJ, 578, L5
Tremonti, C. A., et al. 2004, ApJ, 613, 898
Tytler, D., Fan, X.-M., Burles, S., Cottrell, L., Davis, C., Kirkman, D., & Zuo, L. 1995, in QSO Absorption Lines, ed. G. Meylan (Berlin: Springer), 289
Viel, M., Haehnelt, M. G., & Springel, V. 2004, MNRAS, 354, 684
Viel, M., Matarrese, S., Mo, H.-J., Haehnelt, M. G., & Theuns, T. 2002, MNRAS, 329, 848
Wadsley, J. W., & Bond, J. R. 1997, in ASP Conf. Ser. 123, Computational Astrophysics, ed. D. A. Clarke & M. J. West (San Francisco: ASP), 332
Webb, J. K. 1987, Ph.D. thesis, Univ. Cambridge
Weedman, D. W., Weymann, R. J., Green, R. F., & Heckman, T. M. 1982, ApJ, 255, L5
Weymann, R. J., & Foltz, C. B. 1983, ApJ, 272, L1
Williger, G. M., Smette, A., Hazard, C., Baldwin, J. A., & McMahon, R. G. 2000, ApJ, 532, 77
Young, P. A., Impey, C. D., & Foltz, C. B. 2001, ApJ, 549, 76
Zhang, Y., Anninos, P., & Norman, M. L. 1995, ApJ, 453, L57